

A Bayesian analysis of the experimental evidence underpinning the fourth-power law in shock loading

Cite as: J. Appl. Phys. 137, 245903 (2025); doi: 10.1063/5.0277406

Submitted: 23 April 2025 · Accepted: 22 May 2025 ·

Published Online: 25 June 2025



View Online



Export Citation



CrossMark

Beñat Currutxaga-Lerma^{a)} 

AFFILIATIONS

School of Metallurgy and Materials, University of Birmingham, B15 2TT Birmingham, United Kingdom

^{a)}Author to whom correspondence should be addressed: b.gurrutxagalerma.1@bham.ac.uk

ABSTRACT

The Swegle–Grady fourth-power law, a proposed universal scaling for shock compression in materials, has long guided our understanding of how strain rates relate to peak stresses under extreme conditions. Yet, its empirical basis remains narrow, and experimental data often suffer from variability that obscures the true material response. This study re-examines the law using expanded datasets for fcc Al and bcc Fe, spanning decades of strain rates, to test its universality. We employ a Bayesian framework, combining Gaussian process regression to regularize shock wave profiles with a hierarchical model and Student's t-likelihood to account for inter-run biases and outliers. Our results reveal distinct power-law exponents—2.911 for Al and 2.06 for Fe—challenging the notion of a universal fourth-power scaling and highlighting the influence of material-specific properties like crystal structure. This work underscores the need for robust statistical methods in shock compression studies, offering a reproducible approach that can be applied to other materials and experimental contexts. By clarifying the limits of universality, our findings pave the way for more accurate models of material behavior under extreme conditions, with implications for fields from planetary science to high-speed impact engineering.

28 June 2025 08:07:12

© 2025 Author(s). All article content, except where otherwise noted, is licensed under a Creative Commons Attribution (CC BY) license (<https://creativecommons.org/licenses/by/4.0/>). <https://doi.org/10.1063/5.0277406>

I. INTRODUCTION

Steady shock compression in solids occurs when a shock wave of sufficient magnitude is launched in the solid. If the driving stimulus persists, a steady state may ensue, in which the shock wave maintains its waveform while propagating through the solid.¹ This steady state emerges from a balance between the energy input of the driving stimulus and the internal dissipative mechanisms of the material, as its behavior deviates from ideal elastic, non-dissipative behavior. Consequently, the shocked “Hugoniot” state and its driving waveform serve as unique identifiers of the material’s internal dynamics, reminiscent to how stress-strain curves characterize quasi-static deformation.

One of the most surprising findings in this regard is the apparent emergence of a universality class in the relationship between the strain rate $\dot{\epsilon}$ of the shock wave and the steady-state shock compression stress (hereafter, Hugoniot stress, σ_H) achieved through it. Often called the *fourth-power law* or *Swegle–Grady law*,^{2,3} this relation posits that the fourth power of the peak

shocked stress is always proportional to the *maximum* strain rate of the shock wave that drives it, i.e., $\dot{\epsilon} \propto \sigma_H^4$.

This is a surprising scaling relation, for not only has it been claimed to be universal over a vast class of seemingly dissimilar materials including metals, ceramics, polymers, and amorphous solids alike,³ but also because it denotes a non-linearity of an order so unusually high compared to what a material operating in a viscous regime would display (i.e., $\dot{\epsilon} \propto \sigma_H^1$ vs $\dot{\epsilon} \propto \sigma_H^4$) that the causative, seemingly universal dissipative⁴ mechanisms at play would certainly merit great attention. Indeed, fourth-power relations are unusual in nature and often linked to strong dispersive phenomena as may be the case for instance with the Stefan–Boltzmann relation in thermodynamics,⁵ originating in the dispersion of the energy radiated by a black body over all possible wavelengths; or the classical limit of the Rayleigh–Jeans law⁶ and Planck’s law of blackbody radiation at low frequencies.⁵ Other physically meaningful situations where fourth-power relations arise, as in the near-field of classical fields such as the electromagnetic⁷ or the elastic⁸ fields,

where octopolar field effects may become dominant in the near-field, appear unlikely in this case.

Attempts at explaining this scaling law tend to focus on modeling the visco-plastic behavior of the material,^{3,9} often within the framework of dislocation plasticity.^{10–13} However, because the exponent in the power-law relationship is supposed to be identical across a broad range of dissimilar and not necessarily crystalline materials, Grady³ and others¹⁴ have suggested that these materials must share common features in their response to compression at a fundamental level, despite their microscopic differences. Thus, recent work has focused on attempting to explain the scaling law in terms of more fundamental, material-independent quantities such as the product of the dissipated energy and the shock wave's rise time volunteered by Grady,^{3,9,15} although the explanation still requires invoking the linear equation of state relating shock speed and particle speed in the shocked state. This does not, however, negate past and current interest in verifying whether specific viscoplastic theories satisfy the proposed universality class, for indeed if the latter were true, then all said models ought to obey it; in that sense, the proposed Swegle–Grady law would operate as a necessary benchmark of any shock loading model or simulation, and has indeed been used as such:^{10,11} for instance, Austin and McDowell¹¹ enforced consistency with the Swegle–Grady fourth-power law in their viscoplastic models for Cu, Ni, and Al, using it as a benchmark to calibrate parameter estimation, even though their unconstrained fits suggested a scaling exponent closer to 3.¹¹

In addition, as new experimental evidence arises, it has also been called into question whether the scaling law's own exponent is, in fact, a 4, as originally proposed by Swegle and Grady,² or closer to a 3,¹³ as seemingly implied by the data obtained in at least for some metals,^{10,16–18} and likewise suggested by molecular dynamics simulations of shock loading.¹⁹ Moreover, it is now agreed upon that not all classes of materials share the same scaling exponent: granular^{20,21} and layered²² materials appear to display much smaller exponents,²³ which is both explained by and at the same time belies attempts at explaining this through the homogenization arguments used for metals, as it would signify that internal structure matters in some fundamental way. For these reasons, recently questions as to whether the scaling exponent ought to be regarded as an upper proportionality bound have also been raised,¹⁴ arguing that the universality class may consist of a power-law relation rather than of specific (e.g., $p = 4$) exponents, thereby leaving the scaling's essence yet unresolved.

This paper departs from theoretical speculation to interrogate the empirical basis of the power law itself. A striking limitation in this regard is the scarcity of experimental data underpinning its claims. For example, Grady³ assessed whether vanadium conforms to a fourth-power law using a mere three data points—a sample so sparse that any apparent scaling could easily be coincidental, as three points can always be fitted to a power law. This paucity is not an isolated case; across the field, datasets are often small, constrained by the complexity and cost of shock loading experiments, and also by the difficulties arising from comparing different datasets achieved on the same materials under different experimental conditions. Such limited evidence undermines confidence in the universality of the proposed relationship, particularly when the addition of more data, as explored later in this paper, reveals

exponents deviating from the expected $p = 4$, such as $p \approx 3.01$ for Al and $p \approx 2.06$ for Fe (Sec. V). This suggests that the law's empirical foundation may be more fragile than previously assumed, prompting a critical re-examination of its validity. This study primarily examines weak to moderate shock regimes, with strain rates mostly between 10^5 and 10^9 s^{-1} ; strong shock regimes, where homogeneous defect nucleation may lead to more universal scaling across material classes due to diminished material strengthening effects, are beyond the scope of this work, but merit future investigation.

Compounding this issue are systemic biases inherent in the measurement and derivation of key quantities like strain rate and peak stress. Strain rate, for instance, is typically estimated from the derivatives of Velocity Interferometer System for Any Reflector (VISAR)-derived particle speed profiles—a process fraught with instability due to its ill-posed nature²⁴—and varies in definition across studies, from maximum time derivatives³ to averages based on sample width and sound speed.¹⁸ The VISAR signal itself is interferometry data that must be first regularized to a shock waveform in terms of particle speed and then perhaps further regularized via filters or other techniques.²⁵ All such steps are reasonable and to be expected, but they introduce systemic bias into the reported value of strain rate that must be carefully tracked, something that is often not possible externally in light of published data. Further, the definition of the *peak* stress is likewise ambiguous. For one thing, stress is not directly measured but inferred from particle velocity data via calibrated equations of state, introducing further uncertainty.^{26,27} For another, what it is meant by *peak* is open to ambiguity: is it the maximum stress achieved in a regularized shock waveform that has been converted to stress, or is it a mean stress of said regularized profile corresponding more conventionally to the Hugoniot stress? Added to this, there is the experimental difficulty in sustaining the shocked state for long, as this is caused by an impacting plate or laser ablation, meaning that such peak state may be short lived. And so on. These inconsistencies introduce a pervasive source of systemic bias which, added to the inherent differences of criterion that each author in the literature is bound to follow, complicates comparisons across experiments and challenges the reliability of the resulting scaling exponents. As demonstrated in Sec. IV, even advanced regularization techniques like Gaussian process regression (GPR) struggle to fully mitigate these systemic distortions without robust statistical handling.

Indeed, bias in the form of inter-run variability presents an equally formidable obstacle, arising from differences in experimental conditions such as sample preparation, thickness, purity, and testing protocols. Sources of inter-run bias have long been acknowledged and carefully tackled by the community. Huang and Asay¹⁸, for instance, observed notable biases in aluminum data attributable to sample thickness, while broader studies have highlighted the influence of factors like polycrystallinity^{28–30} and temperature,^{28,31} among many others. This variability manifests as clustering in the data, which is accentuated further by the fact that experimental campaigns tend to focus on a narrow range of strain ranges and stresses, rather than spanning decades thereof. This produces multi-modal distributions that, as we will discuss in this article, a single power law struggles to replicate: Sec. VI reveals how these biases inflate the population of outliers, necessitating heavy-tailed

likelihoods like Student's t to achieve a reasonable fit. Without accounting for such heterogeneity, claims of a universal exponent risk being confounded by artifacts of experimental design rather than reflecting intrinsic material behavior.

Thus, this paper seeks to address these challenges by reinterpreting both prior and new experimental evidence through a Bayesian lens. Bayesian methods, reliant on the modeling of fitting parameters as posterior distributions of the fitting parameter space given the data, afford powerful tools for fitting experimental data to models because they provide a robust framework for quantifying uncertainty and incorporating prior knowledge. These methods excel in handling non-linear models and noisy data, allowing for flexible model comparison and the integration of diverse data sources, ultimately leading to more reliable and interpretable inferences. Such approaches have successfully been used in wide areas of materials science, including among others high-entropy alloy development,³² constitutive modeling of geological materials,³³ or battery lifting,³⁴ to name but a few. Section II introduces a Bayesian methodology anchored in Markov Chain Monte Carlo (MCMC)^{35,36} to obtain statistically robust estimates of the power-law exponent, complemented by diagnostic tests to assess model and data quality. In light of this MCMC framework, the original Swegle and Grady dataset² is scrutinized in Sec. III, where its sparsity is shown to render a power-law relationship statistically tenuous, thereby motivating the need to expand the original datasets in a statistically robust manner. Section IV enhances this analysis with Gaussian process regression (GPR)³⁷ procedure to regularize the shock waveforms and thereby offer a consistent and statistically meaningful way of calculating both the peak stress and strain rate, facilitating the expansion of the datasets in a self-consistent manner that enables the tackling of systemic bias. Leveraging on recently published experimental data, Sec. V applies this refined approach to Al and Fe, providing an expanded dataset with which to perform more reliable MCMC fits using the methodology introduced in Sec. II; this will reveal exponents diverging from $p = 4$ and the probable role inter-run bias plays in the multi-modal clustering of data. Thus, motivated by a wish to understand the role played by inter-run bias, Sec. VI introduces a hierarchical Bayesian model to quantify inter-run variability, showing how Bayesian techniques can be employed to study such effects in a statistically meaningful manner. Finally, Sec. VII summarizes these findings, highlighting the power of modern Bayesian techniques to study and process shock loading data and refine our understanding of the proposed universality class.

II. STATISTICAL MODEL FOR EXPERIMENTAL DATA

The existence of a power law relating the shock (peak) stress to the strain rate can be treated as a simple statistical problem where

$$\dot{\epsilon}_{\text{obs}} = C \cdot \sigma_H^p, \quad (1)$$

where $\dot{\epsilon}_{\text{obs}}$ and σ_H are the strain rate and stress, respectively, both treated as statistical observables (i.e., random variables stemming from some experiment). Here, C is introduced as a

random variable meant to capture experimental uncertainties not explicitly known or reported, and p is the exponent that has been postulated models the relation between the two observables, and likewise treated as a random variable. The parameters C and p would formally be fitted from a single class of experiments, but in practice, owing to the difficulties and limitations involved in acquiring the data, all relevant data for each material must be considered as part of the same set. This introduces both systemic and inter-run variability to the data, which the model, simple as it is, ought to be able to handle if it is to adequately model the phenomenon.

A. A Bayesian inference framework for shock loading data analysis

The presence of systemic and inter-run biases and of otherwise unspecified sources of experimental variability impacts the ability to build predictive models based on the observables alone. However, we have expectations regarding the kind of models that may offer explication for each specific dataset. For instance, for the shock stress-strain rate data, we expect a monotonically increasing relation between them, as experience dictates that a larger strain rate ought to result in a larger shock stress; further, based on prior analyses,^{3,9,15} we expect a power-law relation. This narrows down the possible values our random variables may be expected to take: the C parameter must fall along the positive real line, and the exponent p ought not be very far off unity for otherwise a non-linearity of unusual magnitude would be required to explain the phenomenon, which on its own would question the adequacy of a power-law model. What we seek is a framework with which to further narrow down the model's space until we fully describe the probability distribution functions followed by the model in view of the observable data.

Let us, thus, define the collective variable $\mathbf{x} = \{C, p\}$, which collects the parameters C and p , and let D denote the set of observed data. The set of all possible models will be \mathcal{X} . We are interested in determining the probability distribution function (hereafter "pdf") of the parameters \mathbf{x} given the data D , $p(\mathbf{x}|D)$, to wit, the statistical pdf of the parameters as they appear given the experimental data that are available to us. Bayesian inference enables us to formalize this posterior $p(\mathbf{x}|D)$ via Bayes' rule,

$$p(\mathbf{x}|D) = \frac{p(D|\mathbf{x})p(\mathbf{x})}{p(D)}. \quad (2)$$

Here, $p(D)$ represents the marginal likelihood, and $p(D|\mathbf{x})$, often called the likelihood, represents the pdf of obtaining the data for a given set of parameters \mathbf{x} . $p(\mathbf{x})$ represents the prior pdf for the parameter set, presumably based at least at first on vague knowledge of the values of the parameters. $p(\mathbf{x}|D)$ is called the posterior distribution because it combines prior belief about the parameters' pdf with evidence from the observed data to form an updated belief about the parameter's likelihood.

Thus, Bayes' rule can be thought of as the means through which one updates their beliefs regarding the parameters in light of the data and be used to estimate the parameters and their uncertainty by constructing the pdfs outlined above. This is in practice

28 June 2025 08:07:12

unachievable through analytic means owing to several factors. Crucially, although D represents the observed data, the observed data is a random variable the results of which depend on each particular experiment. Its pdf is formally given by

$$p(D) = \int_{\mathbf{x}} p(D|\mathbf{x})p(\mathbf{x})d\mathbf{x} \quad (3)$$

and is clearly exceedingly difficult to obtain, for it involves integrating over all possible values of \mathbf{x} and has no clear closed-form expression, given that neither of said distributions is available. However, it must be noted that $p(D)$ is a number, and, therefore, it does not affect the shape of the posterior distribution of \mathbf{x} , so it can be regarded as a normalizing constant and ignored in discussions that only aim to compare the relative posterior probabilities of different parameters, in effect justifying regarding $p(\mathbf{x}|D) \propto p(D|\mathbf{x})p(\mathbf{x})$.³⁸ Further, in our particular case, we hold no clear prior beliefs concerning the distribution of the parameter set, so the construction of the likelihood involves the exploration of the values the data may take for all possible values of the parameter space. Thus, if our aim is to obtain the posterior distribution $p(\mathbf{x}|D)$ so as to be able to estimate the value of the parameters given the data, we must use an alternative approach that enables us to sample the model's space and reconstruct said pdf. We will do so via the Markov chain Monte Carlo (MCMC) method.

B. Markov chain Monte Carlo

The Markov chain Monte Carlo (MCMC) method³⁵ uses Markov chains to produce a sequence of samples from the parameter space in such a way that, over time, the distribution of points converges to the target distribution. MCMC has been successfully applied in a vast array of problems, including molecular simulations,³⁹ fitting interatomic potentials for molecular dynamics simulations,⁴⁰ or the constitutive modeling of the plastic response of olivine based on inverse data.^{33,41–43} Crucially, MCMC allows for the estimation of the posterior distribution without needing to know its exact analytical form.

1. Metropolis-Hastings

The procedure that will be employed in this work is a variant of the Metropolis-Hastings (MH) algorithm⁴⁴ comprising the following steps:

- Initialization.** We start with an initial guess \mathbf{x}_0 for the parameter values, either randomly chosen or based on prior knowledge. We further choose a proposal distribution $q(\mathbf{x}'|\mathbf{x})$ that will be employed by the algorithm to suggest a new state \mathbf{x}' given the current state \mathbf{x} . In this case, this proposal distribution will be a normal distribution centered around \mathbf{x} .
- Chain update.** For each iteration t from 1 to N (where N is the total number of iterations desired), we will generate a candidate state \mathbf{x}' by sampling the proposal distribution $q(\mathbf{x}'|\mathbf{x}_t)$ for the current state of the chain \mathbf{x}_t . For each candidate state \mathbf{x}' , we calculate the acceptance probability $A(\mathbf{x}', \mathbf{x}_t)$, which is the probability of moving to the candidate state \mathbf{x}' from the current state \mathbf{x}_t ,

thereby advancing the chain. This probability is given by

$$A(\mathbf{x}', \mathbf{x}_t) = \min\left(1, \frac{p(\mathbf{x}')q(\mathbf{x}_t|\mathbf{x}')}{p(\mathbf{x}_t)q(\mathbf{x}'|\mathbf{x}_t)}\right), \quad (4)$$

where $p(\mathbf{x})$ is the target distribution we are trying to sample from—i.e., the probability distribution of the parameters themselves. If $p(\mathbf{x}')q(\mathbf{x}_t|\mathbf{x}') > p(\mathbf{x}_t)q(\mathbf{x}'|\mathbf{x}_t)$, then the candidate state is certainly better than the current state and is, therefore, accepted and set $\mathbf{x}_{t+1} = \mathbf{x}'$. However, if $p(\mathbf{x}')q(\mathbf{x}_t|\mathbf{x}') < p(\mathbf{x}_t)q(\mathbf{x}'|\mathbf{x}_t)$, we generate a random number u from a uniform distribution over $[0, 1]$. If $u < A(\mathbf{x}', \mathbf{x}_t)$, we still accept the candidate state and set $\mathbf{x}_{t+1} = \mathbf{x}'$. Otherwise, we reject the candidate state and set $\mathbf{x}_{t+1} = \mathbf{x}_t$. The chain of states is Markovian because each element depends solely on the prior element of the chain.

- Burn-in period.** The first few states of the chain may not be representative of the target distribution $p(\mathbf{x})$, especially if the initial guess is far from the equilibrium. These initial samples, which are known as the “burn-in” period of the chain, are usually discarded. In our analysis, we typically deem the first 1000 steps in the chain to be part of this burn-in period

Thus, the Markov chain generates a sequence of samples from the target posterior distribution of model parameters. These samples approximate the joint probability distribution of \mathbf{x} , allowing estimation of the fitting parameter values, their uncertainties, and correlations. Over many iterations, the chain ought to converge to the stationary distribution $p(\mathbf{x}|D)$, providing a robust representation of the parameter space consistent with the observed data and prior knowledge.

2. Hamiltonian Monte Carlo

One of the key disadvantages of Metropolis algorithm as outlined above is that the number of iterations necessary to reach convergence is unknown *a priori*; this can require significant manual tuning of both the number of steps and of the priors and the proposal distribution, especially in high-dimensional spaces, leading to slow convergence and poor sampling performance. As such, it appears desirable to modify the algorithm to increase its performance. One such modification could be to use Gibbs sampling⁴⁵ instead, where the proposal distribution $q(\mathbf{x}'|\mathbf{x})$ is chosen to be the full conditional distribution of the target distribution $p(\mathbf{x})$ with \mathbf{x}' conditioned on all other components, i.e., $q(\mathbf{x}'|\mathbf{x}) = p(\mathbf{x}'|\mathbf{x}) = p(\mathbf{x}) / (\int p(\mathbf{x})d\mathbf{x}')$. This would result in a sampling procedure that requires no tuning and result in a considerably more efficient sampler (q.v.⁴¹). However, in this case, we have not made any assumption regarding the form of $p(\mathbf{x})$, so we must employ an alternative in the form of Hamiltonian Monte Carlo (HMC).⁴⁶

As Gibbs sampling, Hamiltonian Monte Carlo is a variant of Metropolis-Hastings likewise aimed at improving the efficiency of the sampling.⁴⁷ This is achieved by modifying the way the candidate state \mathbf{x}' is selected: whereas conventional MH chooses it at random from a proposal distribution, drawing what is in effect a random walk, HMC seeks to make a more informed proposal for the next sample in the Markov chain by exploiting Hamiltonian mechanics to make a more informed selection of the candidate

state.⁴⁶ The procedure begins by associating each \mathbf{x} parameter state in the chain with a certain linear momentum variable \mathbf{p} , drawn from a normal distribution of mean zero and variance determined by a mass matrix \mathbf{M} —here selected adaptively during the burn-in period. One then constructs a Hamiltonian with potential U and kinetic energies T defined as

$$U(\mathbf{x}) = -\log p(\mathbf{x}|D), \quad T(\mathbf{p}) = \frac{1}{2} \mathbf{p}^T \mathbf{M}^{-1} \mathbf{p}, \quad (5)$$

$$H(\mathbf{x}, \mathbf{p}) = U(\mathbf{x}) + T(\mathbf{p}). \quad (6)$$

For a given state of the chain \mathbf{x}_t , the next candidate state \mathbf{x}' is obtained by updating \mathbf{x}_t and \mathbf{p}_t according to Hamilton's equations, i.e.,

$$\dot{\mathbf{x}} = \frac{\partial H}{\partial \mathbf{p}} = M^{-1} \mathbf{p}, \quad \dot{\mathbf{p}} = -\frac{\partial H}{\partial \mathbf{x}} = \frac{\partial}{\partial \mathbf{x}} \log p(\mathbf{x}|D). \quad (7)$$

Hamilton's equations are integrated over a number of internal time steps that would nominally have to be tuned by the user, and the resulting state \mathbf{x}' (and associated \mathbf{p}') is the desired candidate state. At each new iteration, the momentum \mathbf{p} is resampled to ensure that the exploration of parameter space follows randomized directions. The new state is accepted with the same acceptance probability function, which in this case becomes

$$A(\mathbf{x}', \mathbf{x}_t) = \min\left(1, e^{H(\mathbf{x}, \mathbf{p}) - H(\mathbf{x}', \mathbf{p}')}\right). \quad (8)$$

Because the candidate state is generated by navigating through the gradient of the log-posterior distribution, as HMC advances it is expected to converge considerably faster.⁴⁸ Thus, although each HMC step has greater computational cost than MH (it requires the computation of the gradients to resolve Hamiltonian's trajectory) and still requires tuning, HMC requires fewer samples to converge to the target distribution.

3. No-U-turn sampler

As a means of reducing the need for manually tuning the length of the trajectory integrated over when solving Hamilton's equations, we shall further employ a No-U-Turn Sampler (NUTS),⁴⁹ designed to ensure efficient sampling by preventing the trajectory from unnecessarily retracing its steps by introducing a criterion to stop sampling when the trajectory makes a “*u-turn*.” NUTS uses a recursive algorithm to build a binary tree of potential next states. At each iteration, it randomly decides to expand the tree in either the forward or backward direction in time. This expansion continues until adding another layer to the tree would lead to a *u-turn*. This *u-turn* criterion prevents the sampler from retracing its steps, which would be inefficient and could introduce unwanted correlation between samples. Once the tree is built, a new state (position and momentum) is selected from the tree. The selection process is biased toward states further away in the tree, encouraging exploration of the parameter space. By automatically determining the number of steps to simulate, NUTS removes one of the main barriers to using HMC effectively.⁴⁹

III. MCMC ANALYSIS OF THE ORIGINAL DATASETS

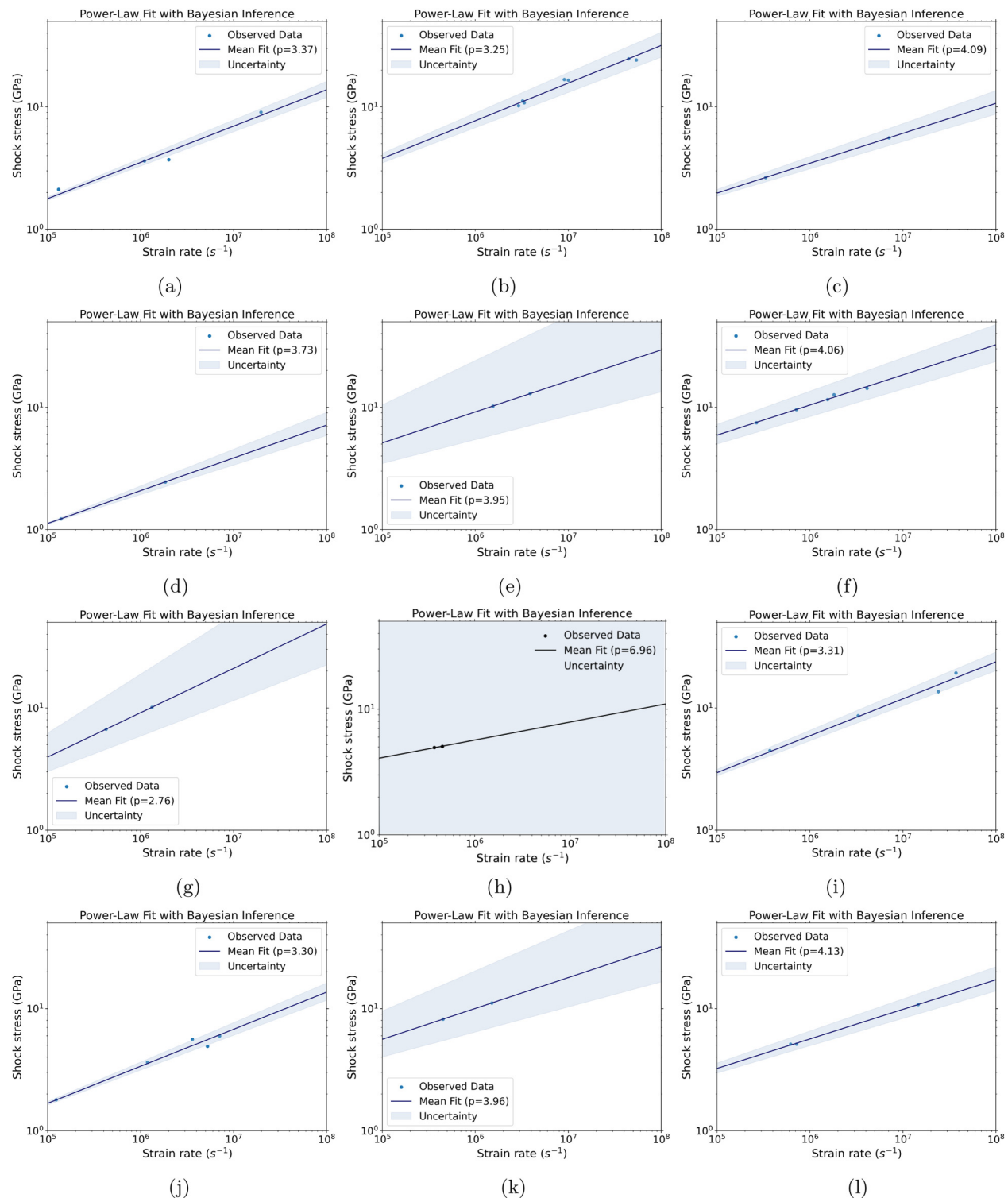
The proposed Bayesian MCMC framework is applied on the original dataset compiled by Swegle and Grady.² To ensure good convergence, the MCMC process was run across 10 chains of 50 000 samples each with a burn-in period of 5000 steps; the model parameters C and p were initialized with a normal distribution of mean 0 and 1 and standard deviation 10^{10} and 10, respectively.

The resulting models are shown in Fig. 1, which depicts the mean model's prediction against the data, and those of its first standard deviations; for greater clarity, Table I collects the mean and standard deviation of the exponent p , alongside results from several statistical tests we describe in Sec. VI. Figure 2 collects the posterior distributions for the exponent p calculated from the MCMC process to showcase the convergence of the process as well as the statistical distribution of the calculated p exponents: as can be seen, most appear to approximate a Gaussian distribution, but unless the mean \bar{p} is very close to 4 (as happens, e.g., for Cu, Mo, U, MgO, and fused silica), the Bayesian model deems a $p \approx 4$ highly unlikely, and typically predicts $p < 4$, which, therefore, arises as an upper bound. These discrepancies with the proposed fourth-power law lead us to assess the quality and appropriateness of the model against a number of statistical tests.

a. Visual inspection via quantile-quantile plots. First, we produce the quantile-quantile (Q-Q) plot of the distribution of residuals⁵⁰ shown in Fig. 3. These Q-Q plots represent the quantiles of the model's predictive distribution on the horizontal x axis, against those expected from a notional normal distribution (as assumed in MCMC) on the vertical y axis. In effect, the Q-Q plot helps visualize how well the model fits the data: as the residuals of the model ought to closely follow a Gaussian distribution, any deviations from the 45° line underlined in red in the plots would signify that the model's predictions are deviating considerably from the expected normality. In this case, all materials are observed to display heavy tails to a greater or lesser degree, which means that outlier data points occur more frequently than expected. For a number of materials, (Al, Be, Mo, soda-lime glass, PBX), their Q-Q plot displays a characteristic S-shaped pattern, indicating that the distribution of empirical data is considerably more leptokurtic than that implied by the model. In essence, the model underestimates the thickness of tails, so predictions made based on the power law might be overly optimistic regarding the rarity of extreme values, or else the data in this case be inordinately affected by systemic bias. This suggests that either the data are full of outliers, or the model (the power law) offers a bad representation of the data, and lacks predictive capabilities.

b. How well does the model match the empirical data? Kolmogorov-Smirnov (K-S) test. We further investigate the adequacy of the mode via the Kolmogorov-Smirnov (K-S) test,⁵¹ which serves to assess the adequacy with which the model (i.e., the power law) actually matches the empirical data. For this, the cumulative distribution function of both the data ($F_{\text{data}}(\mathbf{x})$) and of the associated model ($F(\mathbf{x})$) is calculated. The K-S test then defines the K-S statistic as the supremum of the absolute difference between

28 June 2025 08:07:12



28 June 2025 08:07:12

FIG. 1. Resulting model for the original dataset compiled by Swegle and Grady,² indicating both mean and one standard deviation models predicted by the MCMC Bayesian computation for (a) Al, (b) Be, (c) Cu, (d) Bi, (e) Fe, (f) U, (g) V, (h) quartz, (i) soda-lime glass, (j) PBX, (k) MgO, and (l) fused silica.

TABLE I. Mean (\bar{p}) and standard deviation σ_p of the power-law exponent p , alongside the D -statistic and P -value for the Kolmogorov–Smirnov test performed on the model and dataset. The values of the exponent obtained from fitting the data to the power law with least squares, p_{ls} , are also provided for comparison. As described in Sec. III A, the parameters σ_e and σ_s measure the noise levels the measurements would have to have to produce a fit with $\bar{p} = 4$.

Material	\bar{p}	σ_p	D	P -value	p_{ls}	σ_e (s ⁻¹)	σ_s (GPa)
Al	3.37	0.10	0.25	0.906 25	3.366	5.74×10^5	3.58
Be	3.25	0.11	0.275 4	0.570 51	3.845	1.82×10^6	8.046
Cu	4.09	0.19	0.251 7	0.999 98	4.084	3.73×10^4	0.26
Bi	3.73	0.21	0.250 645	0.999 99	3.730	9.86×10^4	5.58
Mo	3.90	0.31	0.229 4	0.902 31	3.869	6.94×10^4	0.53
U	4.06	0.20	0.200 942	0.960 14	4.975	1.69×10^5	2.59
Fe	3.95	0.60	0.256 696	0.999 64	3.916	2.72×10^5	1.14
V	2.76	0.34	0.255 14	0.999 79	2.743	8.76×10^4	9.25
α -quartz	6.95	4.09	0.268 233	0.997 34	8.675	4.24×10^6	6.47
Soda-lime glass	3.31	0.09	0.249 967	0.906 35	2.003	3.44×10^5	3.045
PBX	3.30	0.10	0.153 121	0.998 38	2.624	4.60×10^5	6.46
MgO	3.96	0.46	0.253 918	0.999 88	3.950	9.80×10^3	0.0069
Fused silica	4.14	0.17	0.182 669	0.999 80	4.130	5.31×10^4	0.032

the empirical cumulative distribution function of the sample and the cumulative distribution function of the reference distribution,⁵¹

$$D = \sup_x |F_{\text{data}}(x) - F(x)|. \quad (9)$$

This provides a measure of the distance between the empirical data and the model's predictions. Typically, a reasonable fit ought to have a small D . The P -value is then calculated as the probability of observing a K-S extreme as the one computed; this is obtained by integrating over the distribution of the KS statistics under the null hypothesis. Typically, we wish to ensure that the null hypothesis is rejected, meaning that there is not enough statistical evidence to conclude that the empirical data's distribution is different from that implied by the MCMC model; this entails a high P -value.

In light of the K-S results presented in Table I, it would, therefore, seem that a power-law model as fitted with MCMC is generally appropriate, in the sense that a reasonable fit can be achieved by using it. Indeed, in this case, D is typically one order of magnitude lower than that of the data ($D \approx 0.25$ for most materials), with high P -value ($P > 0.9$ for most materials). The sole relative outlier (Be) still has a relatively low D value and P -value still sufficiently high ($P = 0.571$) to ensure the null hypothesis is rejected. This suggests that whereas across all materials there is some measurable difference between the model's distribution and the empirical data's, this difference does not appear to be statistically significant, and, therefore, the K-S test results suggest that the power-law model is a good fit for the data.

This test alone seems to support the power-law model, but also suggests that the fitted exponents obtained by the MCMC procedure are adequate, which as may be seen in Table I would reject the proposed universal four power law in favor of $p \approx 3.5$, as the fitted exponents display a variability between $p = 2.76$ for vanadium and $p = 6.95$ for α -quartz. The latter also displays vast variance ($\sigma_p = 4.09$ vs $\bar{p} = 6.95$), which as may be seen in Fig. 1(h) renders the model's predictions for quartz entirely

inadequate, as any empirical data point falling within two decades of stress and three of strain rate of the dataset provided would fall within one standard deviation of the predictions provided by the mean $\dot{\epsilon} \propto \sigma_H^{6.95}$ power law. As indicated above, the posteriors of the exponent p shown in Fig. 2 also highlight the fact that unless $\bar{p} \approx 4$, then it seems statistically unlikely that p would ever be 4.

28 June 2025 08:07:12

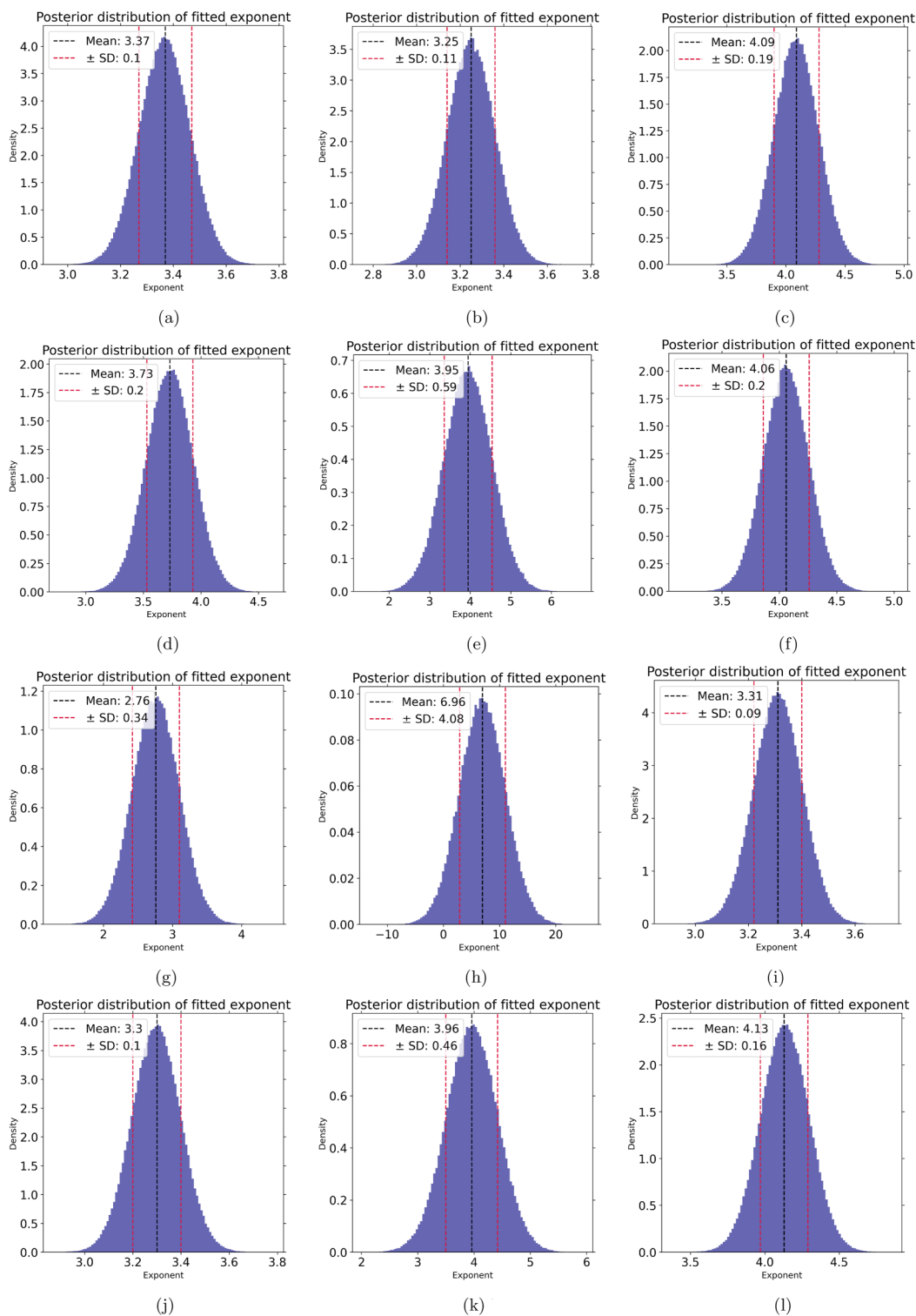
c. How well does the model represent the data? LOO-CV Pareto k test. Further diagnostic metrics are implemented to evaluate the model's adequacy. Within the Bayesian framework, the Pareto k diagnostic test is utilized to examine the model structure and identify outliers in the dataset.⁵² This is facilitated through the leave-one-out cross-validation (LOO-CV) procedure,^{52,53} where each data point is sequentially omitted, and the model is refitted to the remaining data. The model's predictive accuracy is then assessed on the omitted data point, repeating this process for all data points.

During this LOO-CV procedure, the Generalized Pareto Distribution (GPD) is fitted to the tail of the distribution of standardized LOO log-ratios between the actual omitted data point y_i and its predicted value from the LOO-CV model y_{-i} , defined as

$$\text{LogRatio}_i = \frac{1}{\sigma_{\text{LogRatio}}} \left(\ln \frac{p(y_i | \text{model}_{-i})}{p(y_i | \text{model}_{\text{all}})} - \mu_{\text{LogRatio}} \right), \quad (10)$$

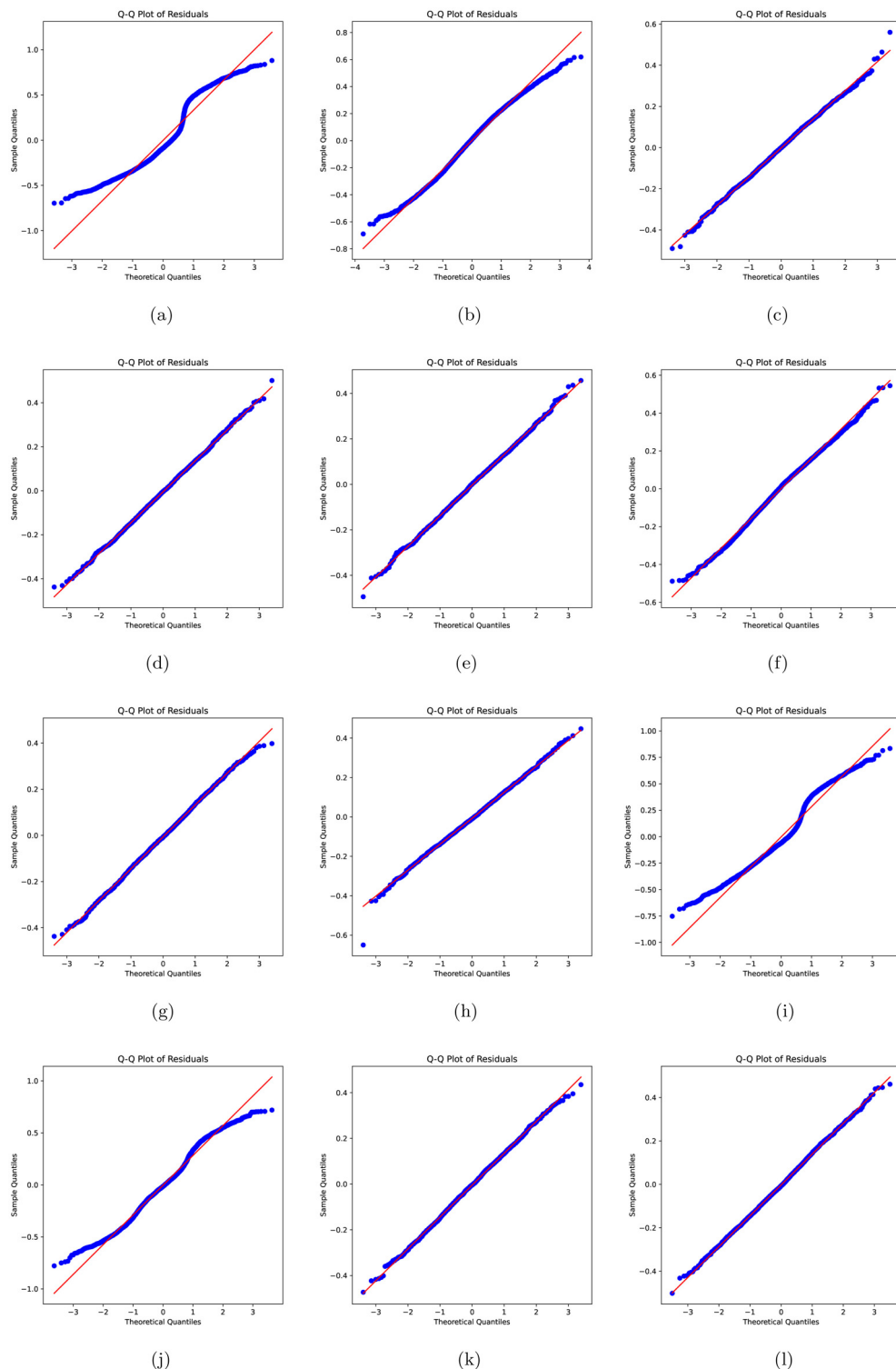
where μ_{LogRatio} and σ_{LogRatio} represent the mean and standard deviation of the LOO log-ratios across all data points, respectively. The largest log-ratios, specifically the top 20% of values,⁵² form the tail of the distribution. This subset is then fitted with a GPD using the maximum likelihood estimation method. The GPD is characterized by three parameters: location (μ), scale (s), and shape (k),

$$f_{\text{GPD}}(x) = \frac{1}{s} \left(1 - k \frac{x - \mu}{s} \right)^{-\frac{1}{1-k}}. \quad (11)$$



28 June 2025 08:07:12

FIG. 2. Posterior distributions of the fitted exponent p , indicating both mean and standard deviations for (a) Al, (b) Be, (c) Cu, (d) Bi, (e) Fe, (f) U, (g) V, (h) quartz, (i) soda-lime glass, (j) PBX, (k) MgO, and (l) fused silica.



28 June 2025 08:07:12

FIG. 3. Q-Q plots for (a) Al, (b) Be, (c) Cu, (d) Bi, (e) Fe, (f) U, (g) V, (h) quartz, (i) soda-lime glass, (j) PBX, (k) MgO, and (l) fused silica. The red $y = x$ line represents the ideal scenario where the sample quantiles (y axis) perfectly match the theoretical quantiles (x axis) of the assumed distribution.

The Pareto k parameter resulting from this fit assesses the shape of the tail of the distribution. For $k > 0$, the distribution exhibits a heavy tail, indicating a higher probability of extreme values compared to light-tailed distributions, such as the Gaussian distribution. This implies that extreme values are more common, often due to the presence of outliers or a model's fundamental misprediction of data points.

The application of the Pareto k diagnostic to various material datasets using the MCMC-fitted power-law model is shown in Fig. 4. Typically, a Pareto k value below 0.5 indicates that the power-law model adequately represents the data's characteristics. Values within the range $k \in [0.5, 0.7]$ suggest an increasing influence of outliers on the model's estimates, whereas $k > 0.7$ indicates that outliers predominate.⁵² The analysis revealed that for most materials, $k > 0.5$ for the majority, if not all, data points, with a substantial number exceeding $k > 0.7$, as shown in Fig. 4. In some cases, such as, e.g., Al [Fig. 4(a)] or Mo [Fig. 4(e)], the k parameter of the data points exceeds unity. Among all evaluated materials, only beryllium (Be) exhibited a significant proportion of data points with $k < 0.5$ —given that Be failed the K-S test, this appears to suggest that the only dataset not formed by outliers does not conform well to a power law.

The application of the Pareto k diagnosis test, therefore, suggests that either all the datasets are formed by outliers, or else that the power-law model offers a statistically inadequate representation of the data. A potential remedy that could be used to save the model could involve excluding data points with high Pareto k values as outliers or statistical anomalies, on the premise that some form of systemic bias may have compromised the data integrity. However, in this particular case, such an exclusion would eliminate a large fraction of the data across most materials, raising concerns about the datasets' suitability and the power-law model's ability to accurately represent underlying data trends. The findings, thus, call into question the model's appropriateness in this context, largely brought about by the scarcity of data points.

A. Quantifying noise levels

The Bayesian analysis conducted in this study indicates that the datasets are statistically unlikely to conform to a power-law model. Furthermore, even if the model were statistically valid, the resulting exponent does not necessarily approximate the proposed value of $p = 4$. This discrepancy, previously highlighted in the literature in the context of aluminum,¹³ could potentially be ascribed to errors in the measurement or subsequent sources of systemic bias introduced in the processing of the experimental raw data. While it is not feasible to address all potential sources of error and their effect in the measurement, we can estimate the noise levels (i.e., the magnitude of the error) that would be required for the observed exponent p to be different from the nominal value of $p = 4$ the fourth-power law posits, as a way of gauging how probable it is that systemic bias alone explains the discrepancy between the fourth-power law and the observed data. As we outline below, there are good statistical reasons to believe that $p = 4$ might be an upper bound and the discrepancies associated with experimental noise in the datasets.

To that end, we propose the following statistical experiment. We assume a known theoretical exponent $p_{\text{true}} = 4$ in a power-law relationship $\dot{\epsilon}_{\text{true}} = C_{\text{true}}\sigma^4$, where $(\dot{\epsilon}_i, \sigma_i)$ are measured data points with $i = 1, \dots, M$. From these data, a MCMC-fitted exponent n_{obs} is found to be less than 4.

We assume that these deviations from the “true” exponent stem from experimental noise in the data, which we model as normally distributed,

$$\dot{\epsilon}_{\text{measured},i} = \dot{\epsilon}_{\text{true},i} + \eta_{\dot{\epsilon},i}, \quad \eta_{\dot{\epsilon},i} \sim \mathcal{N}(0, \sigma_{\dot{\epsilon}}^2), \quad (12)$$

$$\sigma_{\text{measured},i} = \sigma_{\text{true},i} + \eta_{\sigma,i}, \quad \eta_{\sigma,i} \sim \mathcal{N}(0, \sigma_{\sigma}^2). \quad (13)$$

The goal is to find $(\sigma_{\dot{\epsilon}}, \sigma_{\sigma})$ such that synthetic data generated under the assumption $n = 4$ and the above noise model, when fitted, produces an exponent close to n_{obs} . This would indicate that the observed deviation can be explained by measurement noise of these magnitudes.

a. Analytic approximation. Assuming that the noise in σ dominates, it is possible to estimate the variances via the attenuation in linear models.⁵⁴ We consider a log-transformed version of the power law,

$$\ln(\dot{\epsilon}) = \ln(C) + p \ln(\sigma), \quad (14)$$

where the theoretically expected exponent is $p = 4$. If the measured values of σ are perturbed by additive noise, we can write

$$\sigma_{\text{measured}} = \sigma_{\text{true}}e^{\varepsilon}, \quad (15)$$

with ε being a zero-mean noise term. Defining $X_{\text{true}} = \ln(\sigma_{\text{true}})$ and $X_{\text{measured}} = \ln(\sigma_{\text{measured}})$, the observed linear regression in log-log space becomes

$$Y = \ln(\dot{\epsilon}) = \ln(C) + 4X_{\text{true}}, \quad (16)$$

but we only have access to

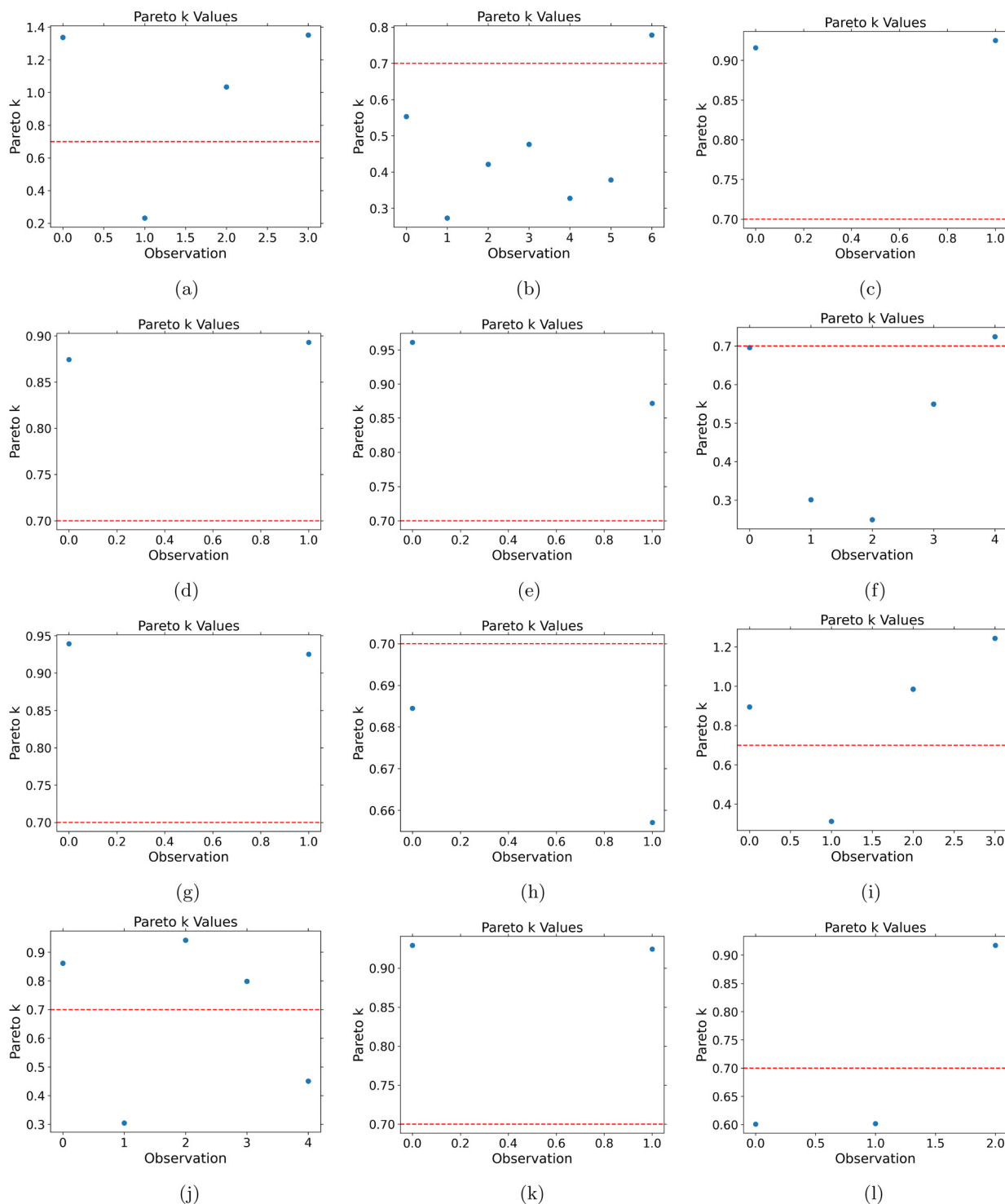
$$X_{\text{measured}} = X_{\text{true}} + \varepsilon. \quad (17)$$

When a linear regression is performed using X_{measured} instead of X_{true} , classical attenuation theory says that estimated slope \hat{p} is reduced relative to its true value due to the presence of noise in the independent variable.⁵⁴ Specifically, the estimated exponent \hat{p} relates to the true exponent (4 in this case) as

$$\hat{p} = 4 \cdot \frac{\text{Var}(X_{\text{true}})}{\text{Var}(X_{\text{true}}) + \sigma_{\varepsilon}^2}, \quad (18)$$

where σ_{ε}^2 is the variance of the additive noise in X_{measured} . We can use this expression to estimate the noise levels in stress required for each material, although the estimate is only accurate if noise levels in strain rate are low. For instance, for Al, $\sigma_{\varepsilon} = 1.1$ GPa; for Fe, $\sigma_{\varepsilon} = 1$ GPa. These values are within the same or one order of magnitude less than the peak stress.

28 June 2025 08:07:12



28 June 2025 08:07:12

FIG. 4. Pareto k diagnosis for (a) Al, (b) Be, (c) Cu, (d) Bi, (e) Fe, (f) U, (g) V, (h) quartz, (i) soda-lime glass, (j) PBX, (k) MgO, and (l) fused silica. Almost all datasets are seen to have $k > 0.5$, and in many cases above the $k > 0.7$ limit beyond which the data points must be considered as outliers. The red lines in the plots indicate the $k = 0.7$ limit of acceptance.

Relevant here is that as the noise level σ_e^2 increases, the ratio

$$\frac{\text{Var}(X_{\text{true}})}{\text{Var}(X_{\text{true}}) + \sigma_e^2} \quad (19)$$

decreases, causing a systematic downward bias in the estimated slope \hat{p} . This is consistent with the observed behavior of most (but not all) power-law exponents, where $p < 4$. In other words, even though the underlying relationship has an exponent of 4, the observed exponent will be less than 4, and this discrepancy can be explained purely by noise in the measured stress values.

b. *An optimization algorithm for estimating the noise levels.* The assumption that the noise in the stress values dominates all other sources of noise does not necessarily extend to all datasets. For one thing, the estimate of the strain rate itself is subject to considerable variations. A more robust estimate of the required noise levels can be achieved through statistical simulation. First, the parameter C_{true} is estimated by imposing $p = 4$ and performing an MCMC fit to the data, using the procedure outlined above but with $p = 4$ fixed. Given candidate noise levels (σ_e, σ_s) , synthetic datasets are generated as follows. For each original point $(\sigma_i, \dot{\epsilon}_i)$, we treat σ_i as $\sigma_{\text{true},i}$ and compute

$$\dot{\epsilon}_{\text{true},i} = C_{\text{true}} \sigma_{\text{true},i}^4. \quad (20)$$

Noisy data are then simulated by drawing random numbers from the corresponding normal distributions for a choice of $\sigma_{\text{sim},i}$ and $\dot{\epsilon}_{\text{sim},i}$, both of which must be optimized as described below. Here, it suffices to say that if $\sigma_{\text{sim},i}$ or $\dot{\epsilon}_{\text{sim},i}$ are non-positive, they are replaced by a small positive number (e.g., 10^{-12}) to allow taking logarithms.

The simulated data $(\dot{\epsilon}_{\text{sim},i}, \sigma_{\text{sim},i})$ are fitted to a power law using MCMC in log–log space,

$$\ln(\dot{\epsilon}_{\text{sim},i}) = \ln(C_{\text{sim}}) + p_{\text{sim}} \ln(\sigma_{\text{sim},i}), \quad (21)$$

yielding an estimated exponent p_{sim} . By repeating this simulation multiple times (e.g., $N = 10^3$) for the same (σ_e, σ_s) , we compute the average simulated exponent,

$$p_{\text{avg}}(\sigma_e, \sigma_s) = \frac{1}{N} \sum_{j=1}^N p_{\text{sim},j}. \quad (22)$$

Owing to the stochastic nature of the noise levels, we expect that $p_{\text{avg}} \neq p_{\text{obs}}$. We define a residual function to measure the discrepancy

$$r(\sigma_e, \sigma_s) = p_{\text{avg}}(\sigma_e, \sigma_s) - p_{\text{obs}}. \quad (23)$$

Also associated with it is an objective function,

$$\chi(\sigma_e, \sigma_s) = |p_{\text{avg}}(\sigma_e, \sigma_s) - p_{\text{obs}}|^2. \quad (24)$$

Minimization of $\chi(\sigma_e, \sigma_s)$ over $\sigma_e, \sigma_s \geq 0$ provides the noise levels that best explain the observed exponent.

1. Minimizing the objective function

We perform the minimization of χ by considering the minimization of the residuals

$$\min_{\mathbf{x}} \sum_{i=1}^N r_i(\mathbf{x})^2, \quad (25)$$

where $\mathbf{x} = (\sigma_e, \sigma_s)$ is the vector of standard deviations, and $r_i(\mathbf{x})$ are the residual functions obtained from each simulation.

The approach we follow here consists of an iterative trust-region method suitable for non-linear least squares problems. At a given iteration \mathbf{x}_k , the algorithm approximates the non-linear residuals $r_i(\mathbf{x})$ by their first-order Taylor expansion around \mathbf{x}_k ,

$$r_i(\mathbf{x}) \approx r_i(\mathbf{x}_k) + \mathbf{J}_{i,*}(\mathbf{x}_k)(\mathbf{x} - \mathbf{x}_k), \quad (26)$$

where $\mathbf{J}(\mathbf{x}_k)$ is the Jacobian matrix with elements $J_{ij} = \partial r_i / \partial x_j$ evaluated at \mathbf{x}_k .

Substituting this linearization into the sum of squares, one obtains a local quadratic model,

$$\sum_{i=1}^N r_i(\mathbf{x})^2 \approx \sum_{i=1}^N [r_i(\mathbf{x}_k) + \mathbf{J}_{i,*}(\mathbf{x}_k)(\mathbf{x} - \mathbf{x}_k)]^2. \quad (27)$$

Defining $\mathbf{r}(\mathbf{x}_k)$ as the vector of residuals at \mathbf{x}_k , and $\mathbf{J}(\mathbf{x}_k)$ as the Jacobian, this quadratic model can be written as

$$\|\mathbf{r}(\mathbf{x}_k) + \mathbf{J}(\mathbf{x}_k)\Delta\mathbf{x}\|_2^2, \quad (28)$$

where $\Delta\mathbf{x} = \mathbf{x} - \mathbf{x}_k$.

In order to choose an adequate $\Delta\mathbf{x}$, we employ the trust-region method,⁵⁵ which constrains $\Delta\mathbf{x}$ to lie within a region (the “trust region”) defined by a radius Δ , typically a ball in parameter space. The step $\Delta\mathbf{x}$ is then chosen to approximately minimize the quadratic model subject to $\|\Delta\mathbf{x}\| \leq \Delta$. After the step is computed, the improvement it achieves in the true objective function is compared against the improvement predicted by the quadratic model,

$$\rho = \frac{\text{actual reduction}}{\text{predicted reduction}} = \frac{\sum_{i=1}^N r_i(\mathbf{x}_k)^2 - \sum_{i=1}^N r_i(\mathbf{x}_k + \Delta\mathbf{x})^2}{\|\mathbf{r}(\mathbf{x}_k)\|_2^2 - \|\mathbf{r}(\mathbf{x}_k) + \mathbf{J}(\mathbf{x}_k)\Delta\mathbf{x}\|_2^2}. \quad (29)$$

If ρ is close to 1, the quadratic model is a good approximation and the step is accepted. If ρ is small or negative, indicating poor agreement between the model and the actual function behavior, the step is rejected or modified, and the trust-region radius Δ is decreased, making the next trial step more conservative.

In order to ensure the stability in the convergence, here we use the Levenberg–Marquardt scheme,^{56,57} which adds a damping term to the approximate normal equations. Instead of directly solving

$$\mathbf{J}(\mathbf{x}_k)^\top \mathbf{J}(\mathbf{x}_k) \Delta\mathbf{x} = -\mathbf{J}(\mathbf{x}_k)^\top \mathbf{r}(\mathbf{x}_k), \quad (30)$$

the method solves⁵⁸

$$(\mathbf{J}(\mathbf{x}_k)^\top \mathbf{J}(\mathbf{x}_k) + \lambda \mathbf{I}) \Delta \mathbf{x} = -\mathbf{J}(\mathbf{x}_k)^\top \mathbf{r}(\mathbf{x}_k), \quad (31)$$

where $\lambda \geq 0$ is a damping parameter. For large λ , the step resembles a small gradient-based move; for small λ , it resembles a Gauss–Newton step. The parameter λ is adjusted based on ρ . A high ρ reduces λ , encouraging steps closer to Gauss–Newton, while a low ρ increases λ , restricting the step and improving stability.

This iterative process continues until convergence criteria are met, such as when the change in parameters or residuals becomes sufficiently small.

a. Results. The statistical simulations and subsequent minimization were carried out using the Ceres library.⁵⁹ For computational convenience, instead of providing analytical derivatives, a numeric differentiation approach was used by instantiating a NumericDiffCostFunction in Ceres, which automatically approximates the Jacobian by finite differences. The estimated noise levels are collected in Table I.

Calculating the level of experimental noise required for $p = 4$ provides valuable insights when compared to known or calculable experimental errors. Aluminum offers the most favorable case for analysis due to its predicted exponent of $\bar{p} = 3.37$. For this case, the data would require experimental errors of $\dot{\epsilon} = 5.74 \times 10^5 \text{ s}^{-1}$ and $\sigma = 3.58 \text{ GPa}$. These values are unusually large for any typical experimental dataset. Although assessing the precise magnitude of error in the original dataset is challenging, it is possible to evaluate similar errors in more recent datasets, such as the one provided by Huang and Asay.¹⁸ In their study, the standard deviation of stress measurements is estimated at 0.1 GPa. When compared to the experimental stress range of [2.11, 9.1] GPa, it becomes evident that achieving such large deviations in noise levels would be improbable under typical experimental conditions. This suggests that noise alone is unlikely to account for the observed deviation, challenging the applicability of the $p = 4$ power law for aluminum and highlighting the need for alternative models or refined experimental techniques.

Furthermore, it is insightful to consider the predicted noise levels for materials with exponents closest to $p = 4$, such as copper (Cu) and iron (Fe). For Cu, the predicted standard deviation in stress is 0.26 GPa, while for Fe, it is 1.11 GPa. These values suggest that a broad range of experimental errors could still yield exponents close to $p = 4$, given the datasets currently available. This observation does not necessarily validate the appropriateness of the power-law model. Instead, it highlights the scarcity of data, which allows for the possibility that even datasets with unacceptably large experimental errors could be fitted to the power-law model and subsequently used to support the fourth-power behavior. This highlights the critical need for high-quality, low-error experimental data to rigorously test and validate such models.

2. Conclusions

The key problem with the power-law model's appropriateness appears to be the paucity of data: for the small number of data points available, much of the systemic bias and uncertainties will

be absorbed by the C constant in the model, which in effect means that for small datasets, any dataset imaginable will conform to any model with some accuracy. This is particularly pathological if the data points are very close to one another, as signified by the model for quartz shown in Fig. 1(h), as may best be seen in Fig. 3(h), which shows the posterior distribution of the exponent for quartz, in which case the predictive capabilities of the power law become entirely subject to statistical noise. Conversely, the material whose dataset is best conformed by the power law, Be, is the material whose dataset is found to be worst fitted by the model. Both of these outliers indicate that no specific model will offer a particularly good representation of the data and would lead to the conclusion that the model is misspecified were not for the fact that the datasets are so small that small fluctuations in the data can lead to apparent deviations from the theoretical distribution, even if the underlying data are consistent with the distribution. Thus, it seems necessary to expand the datasets before any such model can be satisfactorily verified.

IV. DATASETS AND DATA TREATMENT AS SOURCES OF SYSTEMIC AND INTER-RUN BIAS

The results from Sec. III motivate the need for expanding the original dataset compiled by Swegle and Grady²³ as a means of increasing the statistical confidence in the power law as a feasible reductionist model of the peak stress–maximum strain rate relationship. This requires focusing on data that has been published since the original dataset was compiled, and analyzing it in such a way that sources of systemic and inter-run bias are handled in a statistically robust manner.

In this section, we explore the chief difficulties in this regard and develop a Bayesian procedure to extract and analyze maximum stress and strain rates from experimental shock wave profiles.

A. General sources of systemic and inter-run bias

The community has long recognized and documented the challenges posed by systemic and inter-run bias in experimental studies of material shock response.^{18,60–66} This is nevertheless not necessarily framed as a source of inter-run bias as much as a means through which to explore the role specific effects such as microstructure or temperature may have in the shock response of the material. Common sources of inter-run bias include variations in sample preparation and testing conditions, both of which have been extensively explored in the literature. Numerous investigations have specifically examined how testing conditions influence the shock response of materials. For example, the effects of temperature have been widely studied (e.g., Refs. 31 and 67–80), alongside the roles of sample preparation and orientation; these include the influence of polycrystallinity (e.g., Refs. 25, 29, and 81), crystallographic orientation (e.g., Refs. 82–85), or material processing (e.g., Refs. 86 and 87), among others.

Moreover, the evolution of experimental methodologies over decades introduces additional inter-run bias, particularly when compiling data to identify overarching trends, such as those discussed herein. For instance, strain rates in plate impact experiments typically remain below $\approx 10^7 \text{ s}^{-1}$, whereas laser shock experiments span a broader range, from $\approx 10^6$ to 10^9 s^{-1} . This shift in technique,

28 June 2025 08:07:12

combined with improvements in measurement precision and instrumentation—such as advanced velocimetry (e.g., Refs. 88 and 89) and high-resolution imaging (e.g., Refs. 90 and 91)—further complicates direct comparisons across datasets. Additional factors, such as differences in material purity or aging effects (e.g., Ref. 87), may also contribute to variability, warranting careful consideration when interpreting historical and contemporary results.

B. A Bayesian procedure to estimate the maximum strain rate and peak stress in shock loading experiments

In typical shock experiment analyses, peak stress is inferred indirectly from surface displacement measurements obtained via laser interferometry methods such as VISAR.^{88,89} Since the particle velocity is derived through numerical differentiation of displacement data, which is itself derived from the Doppler-induced phase shift in the frequency of the reflected laser light of the VISAR, presented as an interference fringe pattern, this step is inherently ill-posed, necessitating regularization techniques to mitigate noise and stabilize the solution. For instance, Whitley *et al.*²⁵ explicitly demonstrate this procedure by applying a low-pass filter to the raw displacement data, effectively removing high-frequency fluctuations. Subsequently, the stress profile is computed using a suitably calibrated equation of state.²⁷

Of the two parameters of interest to this study, peak stress and strain rate, peak stress is the one least affected by the regularization. This is because although variations in regularization techniques or filtering parameters can introduce minor discrepancies between experimental runs, these variations primarily affect fine-scale fluctuations rather than the peak stress. The peak stress is predominantly governed by macroscopic, high-amplitude features of the shock wave that span temporal and spatial scales substantially greater than typical measurement noise. Therefore, minor variations due to regularization choices, such as slight temporal shifts in the peak's occurrence, do not significantly alter the fundamental magnitude of the maximum stress. This ensures the inferred peak stress remains robust and consistent within an order of magnitude across different experimental methodologies.

Conversely, the estimation of strain rate demonstrates considerable sensitivity to both the choice of regularization method and the inherent temporal resolution of the measurement apparatus. The strain rate, $\dot{\epsilon}$, is intrinsically ambiguous due to the non-constant slope of the shock wavefront during loading. Swegle and Grady² addressed this ambiguity by defining a maximum strain rate, computed as the maximum temporal derivative of specific volume normalized by the specific volume at the Hugoniot elastic limit,⁹²

$$\dot{\epsilon}^{\max} = -\frac{\dot{v}^{\max}}{2u_s}, \quad (32)$$

where u_s is the shock wave speed.

Thus, $\dot{\epsilon}^{\max}$ is acutely dependent on the detailed shape of the shock front, derived directly from the particle velocity profile. Even subtle adjustments in smoothing parameters or sampling rate significantly influence the apparent slope due to the nearly flat

localized regions of the shock front. Further, the enhanced precision of modern instrumentation will invariably result in more accurate strain rate estimates simply owing to greater sampling of the shock wave's rise time. Thus, minor alterations in data processing or instrumentation characteristics can lead to marked fluctuations in the calculated strain rate. Hence, while peak stress remains relatively stable, strain rate estimations are substantially more sensitive to methodological choices and data processing nuances.

Hereafter, we assume the validity of the shock Hugoniot relation $u_s = c_0 + S_1 u_p$, where u_p represents the particle velocity; stress is then obtained via the Rankine–Hugoniot relation $\sigma = \rho_0 u_s u_p$, for ρ_0 the reference material density.²⁷ All parameter values employed here correspond with those tabulated in Ref. 27. Under this assumption, evaluating the maximum strain rate reduces to determining the maximum acceleration from a previously regularized shock wave profile, such as described in Ref. 25. Thus, \dot{v}^{\max} is typically influenced by two sequential regularizations. It is worth stressing out that this choice is made for simplicity—the approach we describe is not altered if a more sophisticated equation of state is employed.

In what follows, we propose a Bayesian approach to rigorously quantify uncertainties inherent in computing \dot{v}^{\max} after the initial regularization (VISAR signal filtering). By employing this method, we systematically produce internally consistent maximum strain rate data points. Our strategy involves digitizing published experimental curves into discrete data points [typically represented in (t, u_p) pairs] and employing Gaussian process regression for smooth interpolation and regularization. This approach facilitates accurate extraction of the maximum particle velocity derivative, \dot{v}^{\max} , ultimately yielding reliable estimates of the maximum strain rate.

C. Gaussian process regression to estimate the maximum particle acceleration

Gaussian Process Regression (GPR) is a Bayesian, non-parametric regression technique that enables probabilistic predictions of outcomes. Unlike classical regression approaches, GPR explicitly models prediction uncertainties,³⁷ rendering it especially advantageous for experimental data analysis where uncertainty estimation is crucial to robust interpretation,^{93,94} as is the case in the current conditions.

A Gaussian Process (GP) is formally defined as a collection of random variables for which any finite subset is jointly Gaussian-distributed.³⁷ In the current case, the GPR will be employed to model the underlying function $u_p(t)$ responsible for generating discrete observational data points (t, u_p) , with t representing time and u_p denoting the measured particle velocity.

A GP is fully determined by its mean function $m(t)$ and covariance function (also termed kernel) $k(t, t')$, given respectively by

$$m(t) = \mathbb{E}[u_p(t)], \quad (33)$$

$$k(t, t') = \mathbb{E}[(u_p(t) - m(t))(u_p(t') - m(t'))]. \quad (34)$$

In the present analysis, we assume a zero-mean function, $m(t) = 0$. This is a common simplifying assumption justified by the

28 June 2025 08:07:12

considerable flexibility of GPs to approximate a wide variety of functions through the appropriate selection of kernels alone.⁹⁵ Furthermore, without explicit prior knowledge about the form of the underlying function—such as positivity or monotonicity constraints—non-informative zero mean constitutes a conservative and neutral starting point.

The choice of kernel $k(t, t')$ is critically influential, directly affecting the model's ability to interpolate and generalize from observed data points to unobserved regions, as well as controlling the predictive uncertainty and smoothness of the resultant function.^{37,95,96} Particularly in the present context—where stable differentiation of the inferred function is essential to reliably estimate the derivative of the particle speed—the kernel must be chosen judiciously, to avoid both overfitting, characterized by excessive adherence to noise we are seeking to regularize, which would lead to ill-posed differentiation problems; and underfitting, where the model fails to capture the underlying dynamics, thus yielding derivative estimates devoid of physical meaning.^{93,96}

1. Kernel selection

For the datasets analyzed in this work, we employ a composite kernel that integrates a radial basis function (RBF) with a Matérn kernel. Such a hybrid approach mitigates the inherent limitations of single-kernel Gaussian process models by simultaneously enforcing differentiability requirements and accommodating local irregularities characteristic of experimental shock wave data.^{37,95}

Specifically, the RBF or *Gaussian* kernel is given by

$$k_{\text{RBF}}(t, t') = \exp\left(-\frac{|t - t'|^2}{2\xi_H^2}\right), \quad (35)$$

where ξ_H is the length-scale parameter. Due to its infinite differentiability and inherent smoothness of Gaussian functions, the RBF kernel is well-suited to modeling continuous underlying trends. This smoothness ensures numerical stability when evaluating derivatives, making it especially suitable for inferring physically meaningful velocity and acceleration profiles from noisy experimental measurements.⁹³

However, while the RBF kernel effectively captures smooth, continuous processes, it struggles to accurately represent localized irregularities or steep gradients, such as the pseudo-discontinuities, which are expected in shock wave experiments involving a dual-wave structure (i.e., the rapid transition between an elastic precursor and subsequent plastic wave front). To address this limitation, we incorporate the Matérn kernel, which introduces an additional flexibility to control the smoothness of the Gaussian process explicitly,⁹⁶

$$k_M(t, t') = \frac{2^{1-\nu}}{\Gamma(\nu)} \left(\frac{\sqrt{2\nu}|t - t'|}{\lambda}\right)^\nu K_\nu\left(\frac{\sqrt{2\nu}|t - t'|}{\lambda}\right), \quad (36)$$

where $\Gamma(\cdot)$ denotes the Gamma function, λ is the length-scale parameter, $\nu > 0$ controls the differentiability, and $K_\nu(\cdot)$ represents the modified Bessel function of the second kind.³⁷ The parameter ν explicitly regulates the smoothness, enabling the Matérn kernel to model both smooth and less regular behavior depending on its

value.^{95,96} For practical purposes, popular choices of ν include $\frac{3}{2}$ and $\frac{5}{2}$, which yield functions sufficiently differentiable for robust differentiation yet still capable of capturing steep gradients or localized irregularities effectively.

By combining the RBF and Matérn kernels into a composite kernel, we achieve a flexible yet robust representation,

$$k_m(t, t') = c[\alpha k_{\text{RBF}}(t, t') + (1 - \alpha) k_M(t, t')], \quad (37)$$

where c is an amplitude scaling constant (effectively serving as a constant kernel) ensuring appropriate magnitude scaling for non-normalized data, and $\alpha \in [0, 1]$ is a mixing parameter adjusts the relative contributions of the RBF and Matérn kernels. Here, the choice of α and the respective kernel length scales (σ_H, λ) is optimized via maximum likelihood estimation,^{37,95} as is explained in the Appendix.

As the pseudo-discontinuities represent rapid changes over extremely short timescales which purely smooth kernels might incorrectly smooth over, this hybrid approach accurately preserves such sharp transitions, thereby allowing both accurate differentiation (essential for particle acceleration computation) and faithful representation of the underlying physical processes that produce abrupt transitions in shock waves.⁹²

2. Fitting the Gaussian process regression model

With a collection of data points (t, u_f) and having selected the kernel combined kernel $k_m(t, t')$, we can proceed to fit a Gaussian Process Regression (GPR) model to the data. This involves using the Gaussian Process (GP) framework to predict the function $u_f(t)$ at new time points t based on the observed data.

28 June 2025 08:07:12

a. Selection of test points. We begin by selecting a set of test points $\{t_*\}_{i=1}^{N^*}$ over which we desire to make a prediction, i.e., the points over which we desire to regularize our data. Given that the resulting estimated data points u_{f^*} will then be used to estimate the maximum derivative $\max u_f(t)$ using numerical differentiation, we will select a much finer grid of test points $\{t_*\}_{i=1}^{N^*}$ than data points $\{t\}_{i=0}^N$ so as to ensure the differentiation is well-posed, i.e., we seek $N^* \gg N$, where N is the total number of experimental data points. In the datasets examined in this work, this typically entailed selecting $\{t_*\}$ to be an order of magnitude larger than $\{t\}$, $N^* \propto 10^1 \cdot N$ over a grid of regularly spaced instants in time across the (t_{\min}, t_{\max}) interval defined by the minimum and maximum instants in time in the data.

b. Formulating the covariance matrix of the experimental data. The first step in GPR proper is the construction of the covariance matrix K^m for the experimental “training” data using the chosen kernel function $k_m(t, t')$. This matrix needs to be calculated only once. If we have N observed data points $\{(t_i, u_{f,i})\}_{i=1}^N$, the covariance matrix K^m will be an $N \times N$ matrix where each element K_{ij}^m is computed as

$$K_{ij}^m = k_m(t_i, t_j) \quad (38)$$

for the i th and j th time points in the dataset, and k_m given by Eq. (37).

c. Incorporating noise to the model. To ensure that the model accounts for the possibility of noise stemming from sources of systematic bias in the experimental data, we follow standard practice in adding a white noise term to the diagonal of the covariance matrix as follows:

$$K_{ij} = K^m_{ij} + \sigma_n^2 \delta_{ij}, \quad (39)$$

where σ_n^2 is the variance of the noise and δ_{ij} is Kronecker's delta (i.e., the identity matrix).

d. Conditioning on experimental data. The essence of GPR is to condition the prior distribution of functions (defined by the GP prior, and represented by the noiseless covariance matrix K^m) on the observed experimental data to obtain a posterior distribution of functions that are consistent with the observations. This largely involves the same Bayesian notions as described already in MCMC: the posterior distribution of u_{f^*} is constructed based on our knowledge of the prior distribution of the experimental data u_f . In this particular case, we assume that the data stems from some normal distribution, and this, therefore, involves using the formula for conditional Gaussian distributions rather than Metropolis–Hastings or similar algorithms where we remained agnostic with regard to the distribution of the data. For our new set of instants in time t_* at which we seek predictions, the predictive distribution of the corresponding values u_{f^*} is quasi-normal and given by

$$u_{f^*} | t_*, t, u_f \sim \mathcal{N}(\bar{u}_{f^*}, \text{cov}(u_{f^*})), \quad (40)$$

where \bar{u}_{f^*} and $\text{cov}(u_{f^*})$ are, respectively, the mean and covariance of the predictions.

The mean of the predictions is given by

$$\bar{u}_{f^*} = K^m(t_*, t)[K]^{-1}u_f, \quad (41)$$

where $K^m(t_*, t)$ is the covariance matrix between the test points t_* and the training (input) points t , which must be computed each time; K the covariance matrix of the training data with white noise; and u_f the vector of experimentally measured values corresponding to the inputs t .

The covariance of the predictions is calculated to assess the uncertainty in the predictions at the test points t_* . It likewise involves both the noise-adjusted covariance matrix K and the covariance matrix K_m as follows:

$$\text{cov}(u_{f^*}) = K^m(t_*, t_*) - K^m(t_*, t)[K]^{-1}K^m(t, t_*). \quad (42)$$

e. Obtaining the predictions. The mean vector \bar{u}_{f^*} provides the predictions for the function values at new time points t_* , while the covariance matrix $\text{cov}(u_{f^*})$ quantifies the uncertainties associated with these predictions. Rather than an iterative process as was the case with MCMC, the assumption that the prediction follows a conditional normal distribution facilitates greatly the efficient computation of the regularized data: the mean \bar{u}_{f^*} and covariance $\text{cov}(u_{f^*})$ of the predictions involve matrix operations alone, which can be efficiently executed over all desired prediction points t_* simultaneously; the actual prediction u_{f^*} are normally distributed

with the aforementioned mean and covariance, and need not even be computed if, as is the case here, we are solely interested in the mean fit and its standard deviation, for which \bar{u}_{f^*} and $\text{cov}(u_{f^*})$ suffice. This batch processing is not only computationally efficient but also convenient for analysis, as it provides a comprehensive view of the model's predictions and uncertainties over the desired range of test points in one go. Of interest here would be the standard deviation associated with the time instant t_i^* : given the $\text{cov}(u_{f_i^*})$ matrix, we need to identify the $\text{cov}(u_{f_i^*})_{ii} = \text{var}(u_{f_i^*})$ diagonal component associated with said time instant, and compute its standard deviation as $\sigma_{u_{f_i^*}} = \sqrt{\text{var}(u_{f_i^*})}$.

f. Calculating the derivatives on the data fit. The pairs $\{(t_{*_i}, \bar{u}_{f_i^*})\}_{i=1}^{N^*}$ represent the fit on the test points, and $\{(t_{*_i}, \bar{u}_{f_i^*} \pm \sigma_{u_{f_i^*}})\}_{i=1}^{N^*}$ the error bounds of the data up to one standard deviation. Given that N^* is large by construction, this was achieved using a simple order 4 finite differences scheme,

$$\dot{u}_{f_i^*} = \frac{u_{f_{i+2}^*} + 8u_{f_{i+1}^*} - 8u_{f_{i-1}^*} - u_{f_{i-2}^*}}{12\Delta t} + O(\Delta t^4), \quad (43)$$

where $\Delta t = \frac{t_{\max} - t_{\min}}{N^*}$ is the grid spacing of the test points. Similarly, the derivative of the uncertainty bounds can be computed by changing $u_{f_i^*}$ for $\bar{u}_{f_i^*} \pm \sigma_{u_{f_i^*}}$.

V. ESTIMATES OF PEAK STRESS AND STRAIN RATE FROM SHOCK WAVEFORMS AND MCMC ANALYSIS OF THE EXPANDED DATA

The procedure described above, consisting of a GPR-based regularization of shock wave profiles and the subsequent differentiation of said GPR for the computation of the maximum particle acceleration v^{\max} , followed by the calculation of the maximum strain rate via Eq. (32), was used to analyze published data for shock wave profiles in fcc Al and bcc Fe, account for more recent data covering several decades of strain rates, thereby expanding considerably the original dataset of two datapoints employed by Swegle and Grady.^{2,15} The procedure followed for hyperparameter selection was reliant on a minimization of the marginal likelihood of the fit and is detailed in the Appendix.

The results of said regularizations, an example of which is provided in Fig. 5 for data obtained from Ref. 97 are collected in Fig. 6 for Al and Fig. 7 for Fe. As can be seen, the error bars (which are scaled in the figures to showcase them in the logarithmic scale) appear to be largely inter-run—i.e., particular datasets display more bias than others, and must, therefore, be ascribed to the systemic bias affecting specific datasets. The disparate nature of the sources likewise gives rise to the question whether inter-run bias is in any way affecting the quality of the data, which we address in detail in Sec. VI.

A. The expanded dataset in fcc Al and bcc Fe

The expanded dataset^{17,25,70,73,80,81,97–111} is then re-analyzed within the MCMC framework employed previously. There are two things to highlight from the results of this analysis, collected in Figs. 6 and 7. First, contrary to Swegle and Grady's proposal, the

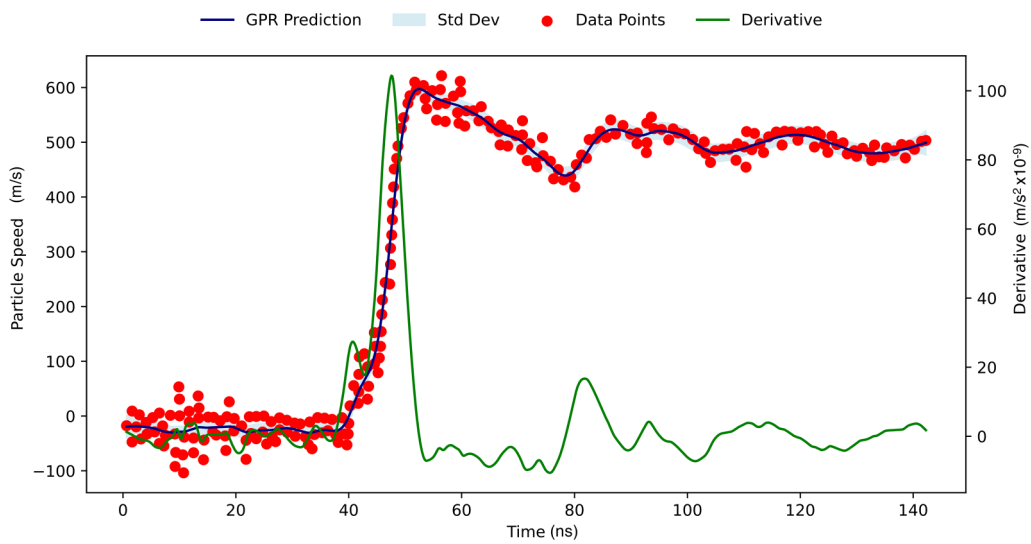


FIG. 5. Results of a Gaussian regression process regularization on Fe data from Ref. 97. The published data are discretized (in red), regularized via GPR with mixing parameter $\alpha = 0.5$, noise parameter $\sigma_n = 500$. The resulting regularization is then differentiated to estimate the particle acceleration, which peaks in the plastic shock front at about $620 \times 10^9 \text{ m/s}^2$. The areas shaded in blue signify regions of up to one standard deviation uncertainty in the GPR fit. As can be seen, the fit is most accurate about the shock wave's raise region, where the maximum slope of the particle speed is obtained. Further, it regularizes noise naturally without the need of filters.

exponent of neither dataset is 4: for fcc Al, the mean exponent is $\bar{p} = 3.01$, leading to what is in effect a third power law, in agreement with prior suggestions by Yao and co-workers;¹³ for bcc Fe, the mean exponent is $\bar{p} = 2.06$ (in effect, a quadratic law), again much lower than originally suggested. On their own, these results call into question whether upon expansion of the datasets, the power-law behavior will be found to be much less non-linear than

originally suggested and, what is more, whether the alleged universality class whereby all materials share said exponent actually exists. This, in turn, would underscore theoretical attempts at explaining it, which have so far yielded so disparate results.^{2,13,15}

Second, as may be seen in (Fig. 8), expanding the dataset has the expected result of narrowing down the exponent's uncertainty, and, excluding some data outliers, a considerable improvement in

28 June 2025 08:07:12

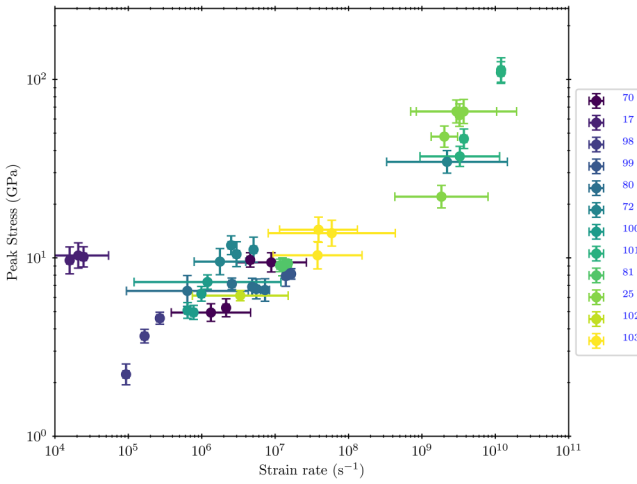


FIG. 6. Strain rate vs peak stress in the expanded and regularized datasets for fcc Al. The error bars have been scaled up by a factor of 10 in stress, and by a factor of 10^3 in strain rate for visualization purposes in the logarithmic scale.

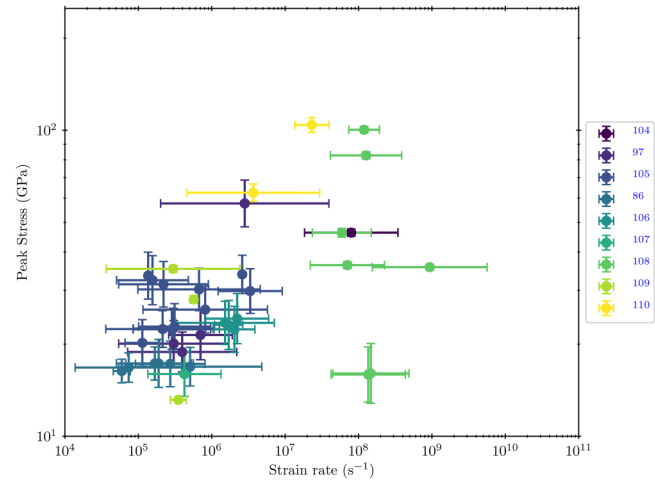


FIG. 7. Strain rate vs peak stress in the expanded and regularized datasets for bcc Fe. The error bars have been scaled up by a factor of 10 in stress, and by a factor of 10^3 in strain rate for visualization purposes in the logarithmic scale.

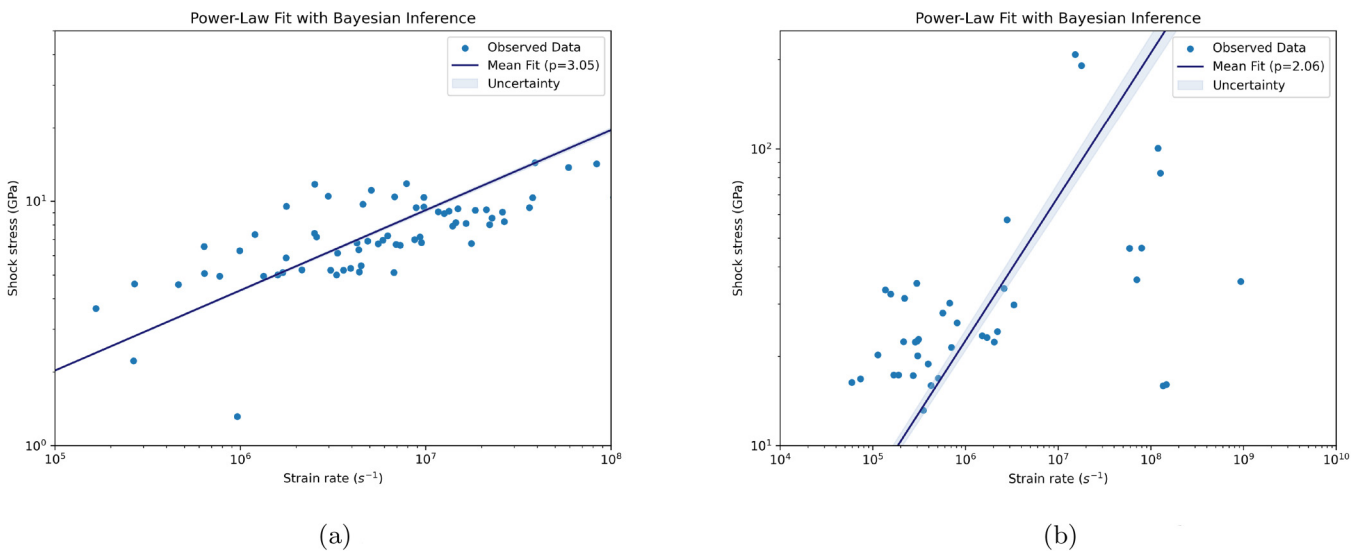


FIG. 8. Revised MCMC fits of Al and Fe using the expanded datasets, both showing significant deviations from the proposed $p = 4$ power-law exponent previously obtained with a much reduced dataset. (a) MCMC fit to revised Al dataset. (b) MCMC fit to revised Fe dataset.

the Pareto k values is achieved over the original datasets [shown in Figs. 9(e) and 10(e), compare them to Fig. 4 of the original analysis]. Still, the data are beset with outliers of extremely high Pareto k , which again demonstrates that the fit is being performed over datasets best with systemic and inter-run bias that merits greater attention, as explored in Sec. VI, to determine whether these discrepancies are due to experimental biases or intrinsic material differences.

B. MCMC diagnostics and the role of data outliers in fcc Al and bcc Fe

Indeed, the posterior predictive checks (PPCs) for the basic MCMC analysis of the power-law model, $\dot{\epsilon} = C\sigma^p$, reveal significant limitations in its ability to reproduce the observed data for both fcc Al and bcc Fe, a discrepancy we attribute primarily to the presence of inter-run biases and outliers. For fcc Al, the observed data values of $\ln \dot{\epsilon}$, plotted against the normalized kernel density estimate (KDE) in Fig. 9(c), exhibit a distinctly multi-modal distribution, with prominent peaks at approximately $\ln \dot{\epsilon} \sim 10$, ~ 15 , and ~ 20 , and troughs at ~ 12 and ~ 17 . Similarly, for bcc Fe, the observed distribution [Fig. 10(c)] shows multi-modality, with peaks at approximately $\ln \dot{\epsilon} \sim 9$, ~ 14 , and ~ 19 , and troughs at ~ 11 and ~ 16 . This multi-modality in both datasets arises from clustering within the data, which we interpret as a consequence of aggregating data from multiple experimental sets, each subject to distinct systematic biases. These biases—potentially stemming from variations in experimental conditions, measurement techniques or sample properties (e.g., purity variations in Fe,¹⁷ differences in Al's crystallographic alignments or sample preparation conditions¹⁸)—manifest as subgroups in the data, each contributing to a separate mode in the distribution of $\ln \dot{\epsilon}$.

In contrast, the posterior predictive distributions of the strain rate for both materials, obtained as the mean KDE from 100 samples of $\dot{\epsilon}_{\text{pred}}$ using a Gaussian likelihood, deviate markedly from the observed distributions, as shown in Figs. 9(c) and 10(c). For Al, the predicted strain rate spans a wider range than the observed data, extending from below $\ln \dot{\epsilon} \sim 7.5$ to beyond ~ 22.5 , while exhibiting fewer distinct modes—dominant peak at ~ 15 , a trough at ~ 20 , and a secondary, less pronounced feature at higher values. For Fe, the predicted distribution similarly overextends, ranging from $\ln \dot{\epsilon} \sim 7$ to ~ 23 , with a primary peak at ~ 14 and a smoother profile that fails to capture the observed peaks at ~ 9 and ~ 19 . Consequently, the predicted distributions for both materials appear overly smooth and overextended, failing to capture the finer multi-modal structure of the observed strain rates. This discrepancy is a direct consequence of the power-law model's functional form: a single power law, $\dot{\epsilon} = C\sigma^p$, assumes a monotonic relationship that cannot naturally produce a multi-modal distribution unless the stress σ itself exhibits such structure—which is unlikely given the typically sequential nature of σ in experimental designs, where higher peak stresses are achieved by increasing projectile speeds or laser intensities. Instead, the model averages over the underlying clusters, yielding broader, less structured distributions that miss the distinct modes induced by inter-run biases.

This observation does not necessarily constitute a direct criticism of the power-law form itself. The multi-modality in the observed data for both Al and Fe may be an artifact of the experimental design or data treatment rather than a reflection of the underlying physical process. The data, being aggregated from multiple sources, are subject to sufficient inter-run biases that the clustering suggested by the multi-modal distributions is likely artificial. In this context, the power law's failure to reproduce the observed distributions could be interpreted as a failure to account for these

28 June 2025 08:07:12

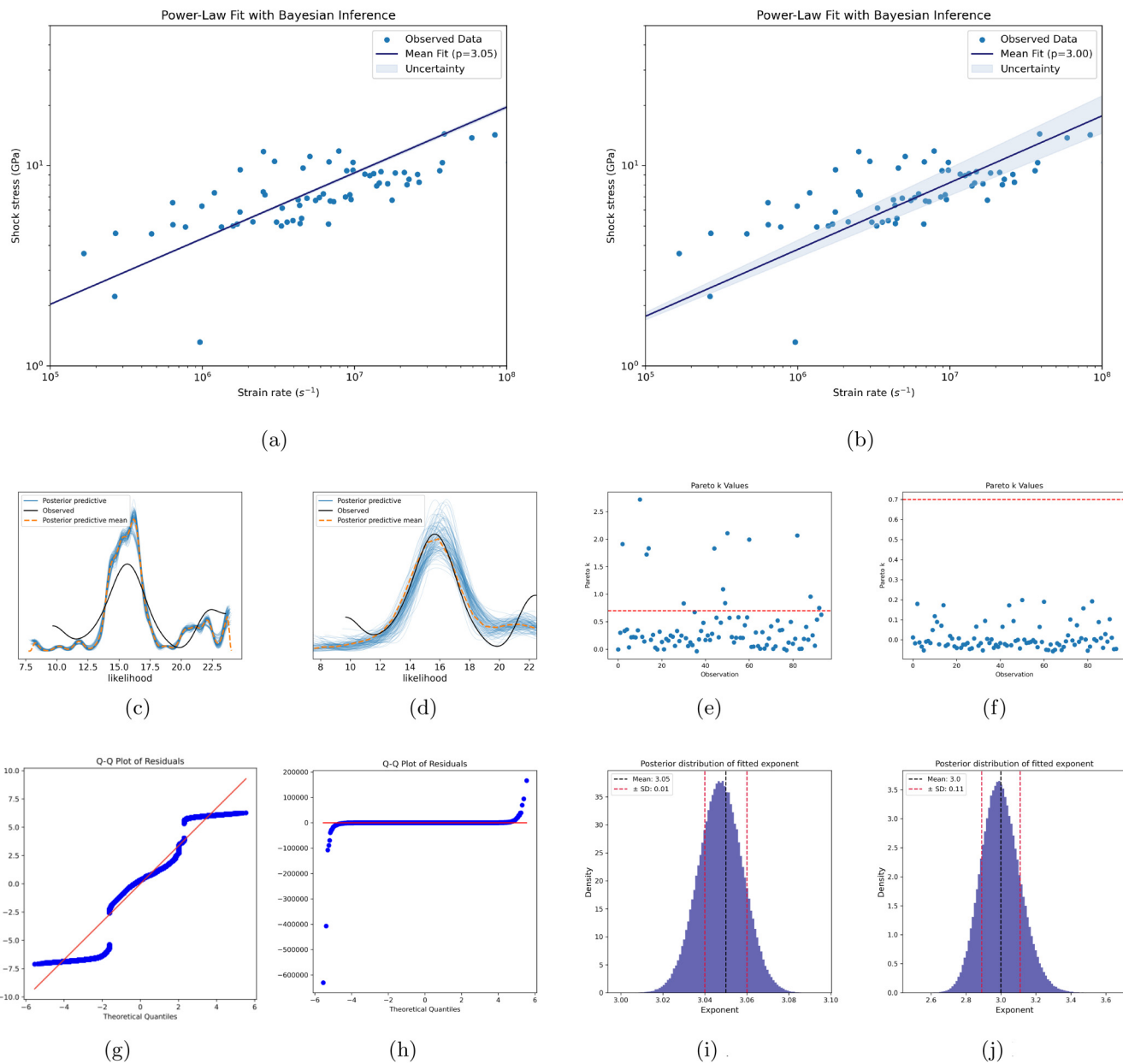


FIG. 9. Paired model diagnostics for the expanded Al dataset using Gaussian and Student's t-likelihoods. Each row compares analogous outputs between models: fit [(a) and (b)], posterior predictive checks [(c) and (d)], Pareto k -diagnostics [(e) and (f)], Q-Q plots [(g) and (h)], and posteriors [(i) and (j)]. In the Q-Q plots, the red line indicates the ideal sample vs theoretical quantiles; in the Pareto k diagnostics, the horizontal red line indicates the acceptance threshold of $k = 0.7$.

biases, compounded by the presence of outliers, rather than a fundamental inadequacy of the power-law form. Further evidence of the model's limitations emerges from the quantile–quantile (Q–Q) plots [Figs. 9(g) and 10(g)] and the Kolmogorov–Smirnov (KS) statistics, which are 0.116 for Al and 0.124 for Fe. These indicate that the power-law model with a Gaussian likelihood cannot adequately

replicate the clustering observed in $\dot{\epsilon}$. The Q–Q plots reveal systematic deviations, with residuals exhibiting heavier tails than expected under a Gaussian assumption, suggesting the presence of outliers or non-Gaussian noise structures in both datasets. The KS statistics, while moderate, further confirm that the observed distributions of $\dot{\epsilon}$ differ significantly from the predicted distributions. This

mismatch is unsurprising: the data for both materials span several decades of strain rate, and the aggregation of multiple experimental sets introduces sufficient outliers and biases that a Gaussian likelihood struggles to accommodate the observed variability. The Gaussian assumption, which implies constant variance and symmetric errors, is ill-suited to capture the heterogeneity and clustering inherent in the data, particularly when inter-run biases amplify the effective noise.

C. Accounting for outliers via Student's t-likelihoods

To strengthen the inference and establish whether the power law's failure to reproduce the data stems from outliers, deviations from the assumed noise structure, or a more fundamental inadequacy of the power-law form, we re-modeled the data using Student's t-distribution for the likelihood, as shown in Figs. 9(d) and 10(d). Student's t-distribution, with its heavier tails controlled by the degrees of freedom parameter v , is better equipped to handle outliers and non-Gaussian noise. For Al, the basic MCMC fit with Student's t-likelihood yields $v = 2.9 \pm 0.2$, while for Fe, it gives $v = 2.8 \pm 0.2$, indicating heavy-tailed distributions for both materials that effectively accommodate their respective outliers. The slightly lower v for Fe may reflect greater experimental noise, such as due to the α - ϵ transition. The results demonstrate a marked improvement for both datasets: the Q-Q plots [Figs. 9(h) and 10(h)] align more closely with the expected straight lines, indicating that the residuals now conform to the assumed noise model. Additionally, the Pareto k -diagnostics [Figs. 9(f) and 10(f)] show improved stability, with all k -values below the critical threshold of 0.7 (most clustering between 0 and 0.2), ensuring reliable leave-one-out cross-validation (LOO-CV) estimates. The PPCs also exhibit better agreement between $\dot{\epsilon}_{\text{pred}}$ and the observed data, with reduced overextension: for Al, $\ln \dot{\epsilon}_{\text{pred}}$ now spans approximately 8–22, and for Fe, 7.5–21.5, closer to the observed ranges, compared to the broader spans with the Gaussian model. Furthermore, the PPCs [Figs. 9(d) and 10(d)] reveal reduced overextension of the predicted strain rate distributions, though the power-law model still fails to capture the multi-modal structure of the observed $\ln \dot{\epsilon}$, with peaks at ~ 10 , ~ 15 , and ~ 20 for Al, and ~ 9 , ~ 14 , and ~ 19 for Fe, as the predicted distributions remain overly smooth. These findings reveal that the datasets for both Al and Fe are inherently dominated by outliers, likely exacerbated by inter-run biases across experimental sets. This appears to be a systemic issue any material will likely be afflicted by, for as in the case of Al and Fe, the datasets can only be expanded by combining data from different experimental campaigns.

Thus, while Student's t-likelihood significantly improves the model's ability to handle outliers in both Al and Fe datasets, it does not address the clustering induced by experimental biases, as the power law remains a single, monotonic model that cannot naturally account for the multi-modality arising from different experimental sets. The differing impacts of outliers on the power-law fits for Al ($\bar{p} = 3.01$) and Fe ($\bar{p} = 2.06$) further suggest material-specific sensitivities: for Al, outliers primarily inflate the variability in C , while for Fe, they may contribute to the lower exponent, possibly due to high-strain-rate conditions where twinning dominates²⁸ or where the $\alpha - \epsilon$ phase transformation has taken place. As a result, any fitting exercise aimed at inferring the existence of a universality

class—where the power-law exponent p is expected to be consistent across conditions—is bound to be confounded by these inter-run biases. The multi-modal nature of the observed $\ln \dot{\epsilon}$ distributions, driven by experimental heterogeneity, suggests that the power law's apparent failure may be an artifact of the data collection process rather than a refutation of its theoretical validity. To rigorously test the universality hypothesis, a more sophisticated model that explicitly accounts for inter-run biases is required, motivating the exploration of hierarchical Bayesian models in Sec. VI.

VI. BAYESIAN ANALYSIS OF INTER-RUN VARIABILITY IN SHOCK RESPONSE

The proposed universality class for the power-law relationship $\dot{\epsilon} = C\sigma^p$ relies on the consistency of the exponent p across diverse experimental sets. However, our Bayesian analysis has shown that the failure of the model to reproduce the data is deeply affected by the presence of inter-run bias—systematic differences arising from variations in experimental conditions, measurement protocols, or material properties (q.v., e.g., Refs. 18 and 60–66). This manifests in a large population of data outliers that could only be handled by expanding the tail of the likelihood via Student's t distributions. This approach has been shown to successfully lead to a higher quality fit, but the fact outliers must be accounted for by heavier tailed distributions can obscure this consistency, potentially leading to erroneous conclusions about universality.

To address this challenge, here we develop a *hierarchical* Bayesian model⁹⁸ with Student's t-likelihood, designed to quantify the effect of inter-run biases on the exponent p while testing the universality hypothesis. The hierarchical model will use data from the expanded experimental sets, each data source comprising measurements of strain rate, stress, and their uncertainties, as recorded in Fig. 6. In a nutshell, the hierarchical model is a MCMC fit (similar to that detailed in Sec. II) that is applied over each individual dataset, but with hyperparameters shared by all of them. In the following, we detail the model's construction and rationale, followed by an in-depth analysis of the results and their implications for the universality class.

28 June 2025 08:07:12

A. Hierarchical Bayesian model construction

The hierarchical Bayesian model is designed to capture the power-law relationship $\dot{\epsilon} = C\sigma^p$ while allowing parameters to vary across experimental sets to account for inter-run biases. For each dataset $j \in \{1, \dots, N\}$, we define source-specific parameters C_j and p_j , representing the scaling constant and power-law exponent, respectively. To ensure numerical stability, we work in the log-transformed space, scaling the data by geometric means: $\log \dot{\epsilon}' = \log(\dot{\epsilon}/\bar{\dot{\epsilon}})$, $\log \sigma' = \log(\sigma/\bar{\sigma})$, where $\bar{\dot{\epsilon}}$ and $\bar{\sigma}$ are the geometric means of the strain rate and stress across all observations. The model for the i th observation in set j is then

$$\log \dot{\epsilon}'_i = \log C_j + p_j \log \sigma'_i + e_i, \quad (44)$$

where e_i represents the error term. The hierarchical structure is introduced by assuming that the source-specific parameters $\log C_j$

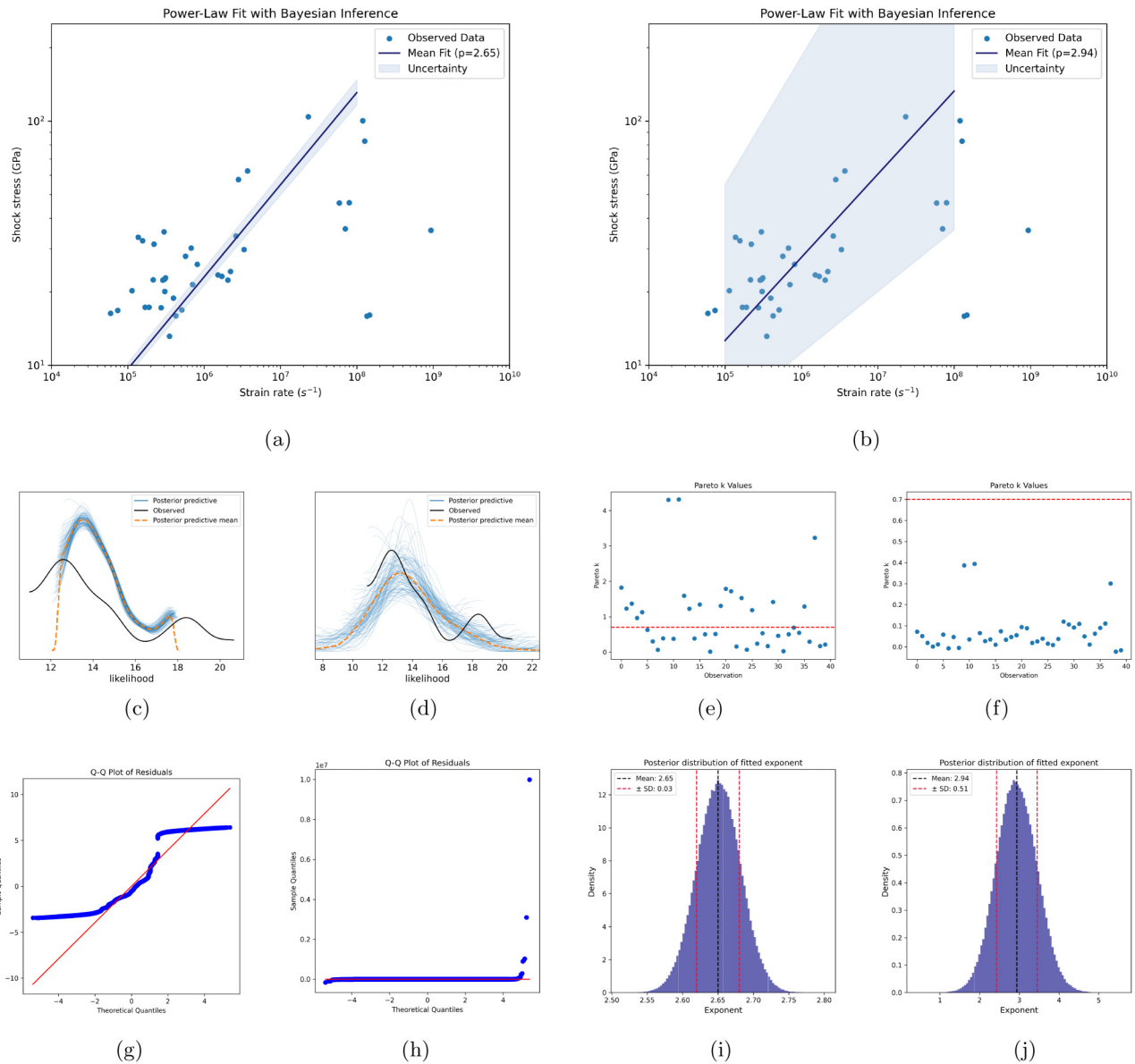


FIG. 10. Paired model diagnostics for the expanded Fe dataset using Gaussian and Student's t-likelihoods. Each row compares analogous outputs between models: fit [(a) and (b)], posterior predictive checks [(c) and (d)], Pareto k -diagnostics [(e) and (f)], Q-Q plots [(g) and (h)], and posteriors [(i) and (j)]. In the Q-Q plots, the red line indicate the ideal sample vs theoretical quantiles; in the Pareto k diagnostics, the horizontal red line indicates the acceptance threshold of $k = 0.7$.

and p_j are drawn from common distributions,

$$\log C_j \sim \mathcal{N}(\mu_{\log C}, \sigma_{\log C}^2), \quad p_j \sim \mathcal{N}(\mu_p, \sigma_p^2), \quad (45)$$

with hyper-priors $\mu_{\log C} \sim \mathcal{N}(0, 1)$, $\sigma_{\log C} \sim \text{Half - Normal}(0.5)$, $\mu_p \sim \mathcal{N}(1, 0.5)$, and $\sigma_p \sim \text{Half - Normal}(0.2)$. These priors are chosen to be weakly informative, allowing the data to dominate the

inference while providing regularization. A non-centered parameterization is employed to improve sampling efficiency: $\log C_j = \mu_{\log C} + \sigma_{\log C} z_{\log C,j}$, $p_j = \mu_p + \sigma_p z_{p,j}$, where $z_{\log C,j}, z_{p,j} \sim \mathcal{N}(0, 1)$.

The error term ϵ_i is modeled using Student's t-distribution to accommodate the heavy-tailed nature of the data, which is evident from the presence of outliers in preliminary analyses. The degrees of freedom v_j are allowed to vary across sets to capture potential

28 June 2025 08:07:12

differences in noise characteristics,

$$\begin{aligned} v_j &\sim \mathcal{N}(\mu_v, \sigma_v^2), \quad \mu_v \sim \mathcal{N}(3, 0.2^2), \\ \sigma_v &\sim \text{Half-Normal}(0.1), \end{aligned} \quad (46)$$

with a non-centered parameterization $v_j = \mu_v + \sigma_v z_{v,j}$, $z_{v,j} \sim \mathcal{N}(0, 1)$. The likelihood for the i th observation in set j is

$$\log \dot{\epsilon}'_i \sim \text{Student-t}(v_j, \mu_i, \sigma_{\text{total},i}), \quad (47)$$

where $\mu_i = \log C_j + p_j \log \sigma'_i$, and $\sigma_{\text{total},i} = \sqrt{\sigma^2 + \sigma_{\dot{\epsilon},i}^2}$ combines the model noise $\sigma \sim \text{Half-Normal}(0.5)$ with the measurement uncertainty $\sigma_{\dot{\epsilon},i}$ propagated to the log scale via $\sigma_{\dot{\epsilon},i} = \sigma_{\dot{\epsilon},\text{raw},i}/\dot{\epsilon}_i$.

The hierarchical structure is motivated by the need to account for inter-run biases, which manifest as systematic differences in C_j and potentially p_j across experimental sets, while testing the universality hypothesis that p_j values are consistent (i.e., σ_p is small). Student's t-likelihood is chosen over a Gaussian to better handle outliers, as the preliminary analysis in Sec. V C indicated heavy-tailed residuals. The varying v_j allows flexibility in the noise model, capturing potential differences in outlier prevalence across sets. Posterior inference is performed using Markov chain Monte Carlo (MCMC) sampling with 25 000 iterations and 5000 tuning steps ensuring convergence as verified by diagnostic metrics.

B. Analysis of inter-run variability and power-law consistency

The hierarchical Bayesian model yields robust insights into the power-law behavior ($\dot{\epsilon} = C\sigma^p$) across experimental sets for fcc Al and bcc Fe. For Al, the hyperparameters indicate a mean exponent $\mu_p = 2.911 \pm 0.133$ (95% highest density interval (HDI): [2.660, 3.164]) with low variability ($\sigma_p = 0.114 \pm 0.089$, 95% HDI: [0.000,

0.274]). For Fe, the model gives $\mu_p = 2.06 \pm 0.15$ (95% HDI: [1.77, 2.35]) with similar consistency ($\sigma_p = 0.12 \pm 0.09$, 95% HDI: [0.00, 0.29]). The tight clustering of p_j around their respective means suggests a consistent exponent within each material, supporting a material-specific power-law scaling. However, the significant difference between Al ($\mu_p \approx 2.911$) and Fe ($\mu_p \approx 2.06$) challenges a universal exponent across materials. This discrepancy likely reflects material-specific factors, such as Al's fcc structure enabling uniform plastic flow, contrasted with Fe's bcc structure, which is prone to twinning at high strain rates²⁸ and further experiences a phase transformation from α -Fe to ϵ -Fe at about 13 GPa.²⁷

Inter-run biases, arising from variations in experimental conditions like sample preparation or measurement techniques (e.g., Refs. 18 and 63), are addressed through the hierarchical structure, which models source-specific parameters C_j and p_j . For Al, the mean log-scaling constant is $\mu_{\log C} = 0.256 \pm 0.172$ (95% HDI: [-0.079, 0.568]), with variability $\sigma_{\log C} = 0.18 \pm 0.11$. For Fe, it is $\mu_{\log C} = 0.117 \pm 0.446$ (95% HDI: [-0.722, 0.963]), with $\sigma_{\log C} = 0.20 \pm 0.10$, reflecting greater heterogeneity, possibly due to sample impurities.¹⁷ The wider credible interval for Fe's $\mu_{\log C}$ suggests more pronounced inter-run biases, exacerbated by its α -to- ϵ phase transition at \sim 13 GPa, which may disrupt the power-law's monotonicity. Student's t-likelihood mitigates the impact of outliers—often artifacts of these biases—by accommodating heavy-tailed residuals, ensuring that inferred parameters reflect intrinsic material behavior rather than experimental noise.

Student's t-likelihood parameters confirm the model's robustness. For Al, the degrees of freedom are $\mu_v = 2.912 \pm 0.196$ (95% HDI: [2.539, 3.282]) with minimal variability ($\sigma_v = 0.002 \pm 0.062$, 95% HDI: [0.000, 0.194]). For Fe, $\mu_v = 2.90 \pm 0.20$ (95% HDI: [2.51, 3.29]) with $\sigma_v = 0.01 \pm 0.05$ (95% HDI: [0.00, 0.11]). These low μ_v values indicate heavy-tailed distributions, consistent with outlier-dominated datasets, while Fe's slightly higher σ_v reflects

28 June 2025 08:07:12

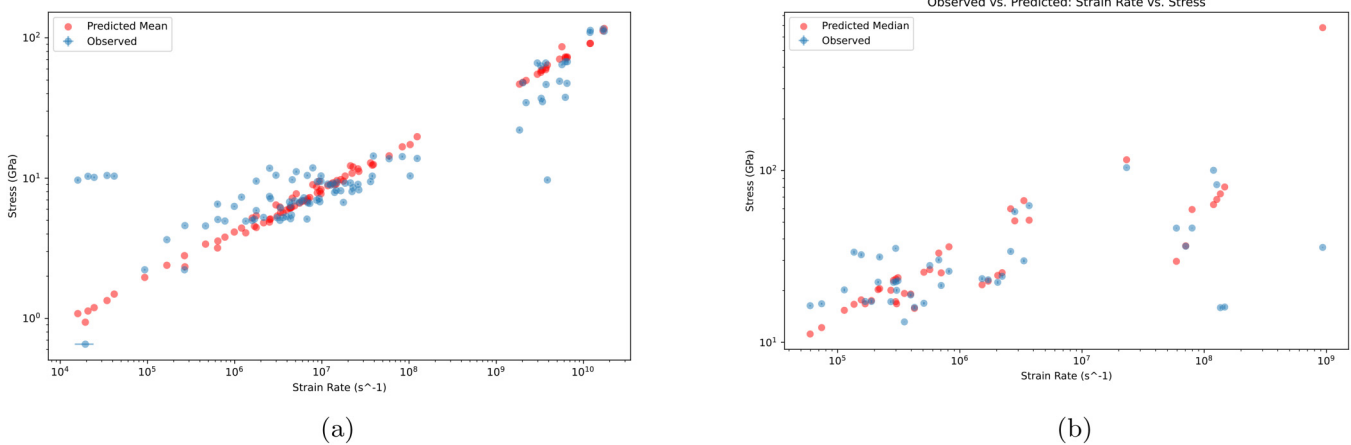


FIG. 11. Observed maximum strain rate vs peak stress (blue points with error bars, typically two to three orders of magnitude smaller than the point) in comparison to posterior predictive means (red dots) from the hierarchical Bayesian models in (a) Al and (b) Fe.

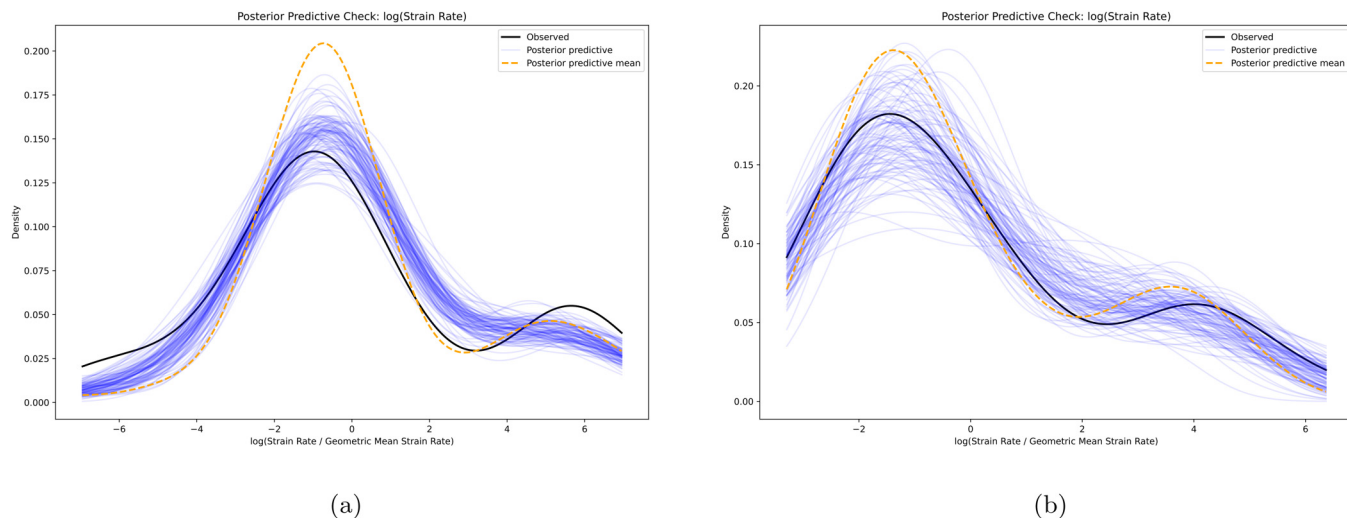


FIG. 12. Posterior predictive checks for the hierarchical Bayesian models of (a) Al and (b) Fe.

greater experimental variability. The scale parameters ($\sigma = 0.068 \pm 0.095$ for Al, $\sigma = 0.07 \pm 0.09$ for Fe) appear small, but diagnostic plots validate the noise model's appropriateness.

Diagnostic plots substantiate the model's performance. The observed vs predicted plot (Fig. 11) shows close alignment on a log-log scale, indicating a good fit. Posterior predictive checks (PPCs, Fig. 12) reveal multi-modal distributions for $\ln \epsilon$, with Al exhibiting peaks at ~ 10 , 15, and 20, and Fe showing distinct peaks due to its experimental conditions. This confirms the model's ability to capture dataset heterogeneity without over-smoothing, a

key improvement over non-hierarchical models. Pareto k -values (Fig. 13), all below 0.7, ensure reliable leave-one-out cross-validation (LOO-CV). Q-Q plots (Fig. 14) align residuals closely with Student's t-distribution ($v \approx 2.912$ for Al, $v \approx 2.90$ for Fe), with minor tail deviations reflecting the heavy-tailed nature of the data.

The hierarchical model isolates inter-run biases by estimating source-specific C_j and p_j , revealing their impact through the posterior variability of $\log C_j$. For Al, $\sigma_{\log C} = 0.18 \pm 0.11$ (95% HDI: [0.05, 0.36]) indicates moderate bias, likely from differences in laser

28 June 2025 08:07:12

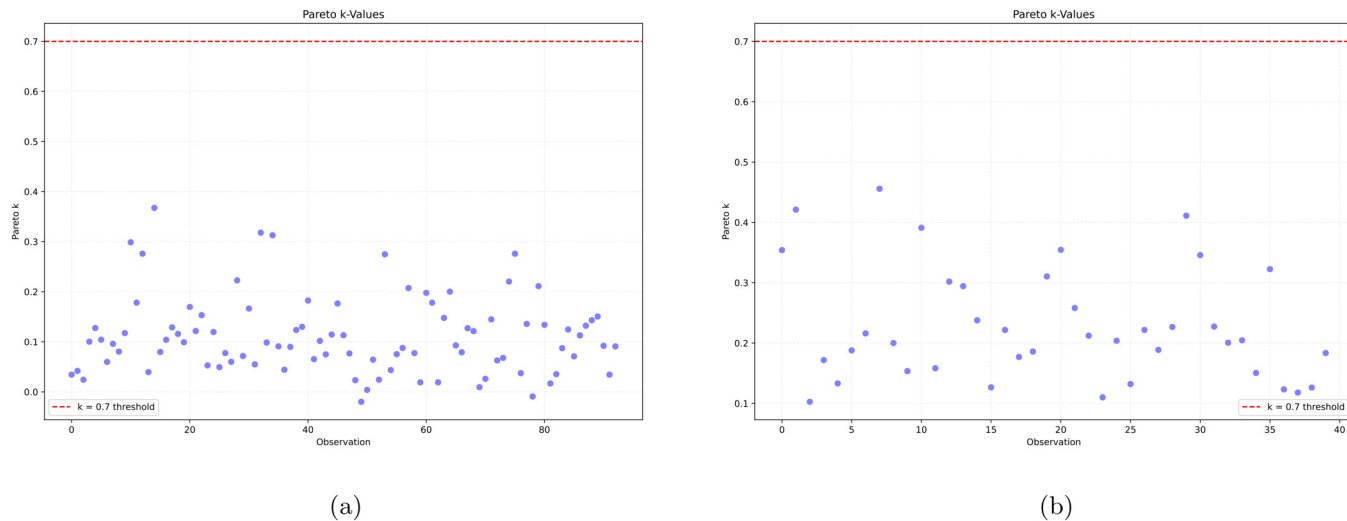


FIG. 13. Pareto k diagnostics for the hierarchical Bayesian models of (a) Al and (b) Fe. The horizontal red line indicates the acceptance threshold of $k = 0.7$.

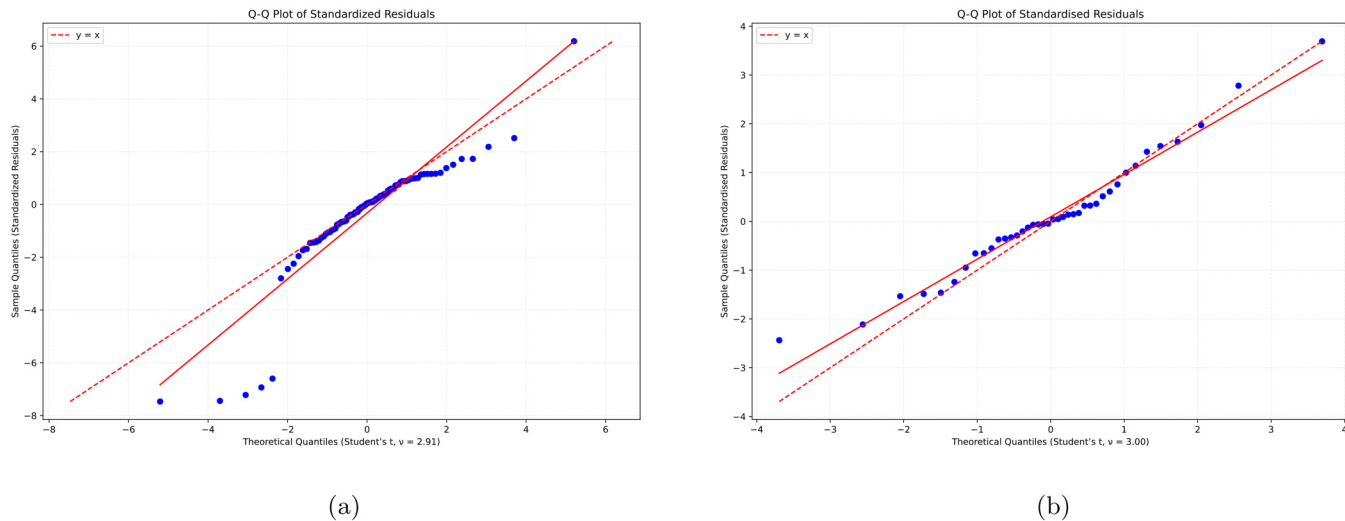


FIG. 14. Q-Q plots for the hierarchical Bayesian models of (a) Al and (b) Fe. The solid line is a linear fit of the quantile points, added to ease the comparison with the sample vs theoretical quantile dashed line.

shock setups.⁸⁰ For Fe, $\sigma_{\log C} = 0.20 \pm 0.10$ (95% HDI: [0.06, 0.39]) suggests slightly higher variability, possibly due to phase transitions or measurement inconsistencies. The tight σ_p for both materials (0.114 ± 0.089 for Al, 0.12 ± 0.09 for Fe) confirms that biases primarily affect scaling constants, not the exponents, preserving the power-law's consistency within each material. Student's t-likelihood further addresses biases by reducing the influence of outliers, ensuring robust p_j estimates, as evidenced by the PPCs (Fig. 12) capturing multi-modal structures without distortion.

To assess inter-run biases' impact, we analyzed diagnostics as detailed in Sec. II. Pareto k -diagnostics (Fig. 13) and Q-Q plots (Fig. 14) confirm the model's reliability, with residuals aligning with Student's t-distribution, validating the heavy-tailed likelihood for handling bias-induced variability. The low σ_p values support consistent exponents within materials, but the distinct μ_p values (2.911 for Al, 2.06 for Fe) suggest material-specific scaling, challenging a universal power law across classes.²³

These results highlight the efficacy of hierarchical Bayesian methods in disentangling inter-run biases from intrinsic material properties. The variability in C_j underscores the need to account for experimental factors like instrumentation⁸⁸ or sample heterogeneity.²⁹ The differing exponents for Al and Fe challenge the Swegle-Grady fourth-power law's universality, suggesting crystal structure or deformation mechanisms govern the scaling, rather than more fundamental dissipative processes common to all classes of non-granular, non-layered materials. This aligns with prior attempts at explaining the scaling by modeling the material's viscoplastic behavior,^{3,9} often within the framework of dislocation plasticity,^{10–13} as this would make the material's scaling inherently dependent on the material's deformation mechanisms active across the decades of strain rate over which said scaling is being proposed.

Crucially, the hierarchical MCMC model excels in isolating and quantifying inter-run biases, enabling statistically robust fits

that accurately reflect material-specific behavior while mitigating the confounding effects of experimental variability. This approach represents the optimal framework for analyzing complex experimental datasets, as it systematically separates systemic and inter-run biases from intrinsic physical relationships, even for ostensibly simple models like the shock power law $\dot{\epsilon} = C\sigma^p$. Because of the hierarchical structure and heavy-tailed Student's t-likelihood, this method ensures that inferences are both precise and resilient to outliers, setting a standard for rigorous data analysis in material science. Its versatility suggests it can be readily extended to other systems where experimental noise and biases obscure underlying physical laws, making it an indispensable tool for future investigations. Future work could incorporate covariates like temperature or polycrystallinity^{25,31} to refine bias estimates and explore power-law applicability across other materials.

VII. CONCLUSIONS

This study has provided a comprehensive re-evaluation of the Swegle-Grady *fourth-power law*, a proposed universality class for the power-law relationship $\dot{\epsilon} = C\sigma^p$ in steady shock compression across diverse materials, through the lens of advanced Bayesian statistical methods. By addressing the critical role of inter-run biases and systemic variability in experimental shock loading data, our work underscores the necessity of robust statistical frameworks to test fundamental hypotheses in material science. Through careful statistical analysis, we have shown that the power-law exponent varies between materials: for fcc Al, it centers at 2.911 with a small uncertainty of 0.133, while for bcc Fe, it falls to 2.06 with an uncertainty of 0.15. These findings, derived from expanded datasets spanning decades of strain rates, challenge the universality of the fourth-power law as initially posited by Swegle and Grady,² revealing that the exponent is not universal but depends on the material's

28 June 2025 08:07:12

intrinsic properties, such as its crystal structure and deformation mechanisms. This challenges the notion of a single fourth-power law governing all materials.

The significance of this work lies in its ability to address a long-standing gap in the shock compression literature: the paucity of statistically robust methods to evaluate the adequacy of power-law models amidst experimental variability. Shock loading experiments are notoriously challenging, with data often plagued by inter-run biases arising from differences in sample preparation, testing conditions, and measurement techniques, as well as systemic biases introduced during data processing (e.g., strain rate estimation from VISAR data). These biases can obscure the true underlying physics, leading to potentially erroneous conclusions about universality classes that are critical for predictive modeling, material design, and understanding dissipative mechanisms in extreme conditions. By employing a hierarchical Bayesian framework, we have not only quantified the impact of inter-run biases on the exponent p but also provided a methodology to disentangle these biases from intrinsic material responses. This is of paramount importance to the material science community, as it ensures that claims of universality—often used as benchmarks for visco-plastic models and simulations^{10,11}—are grounded in statistically sound evidence, thereby enhancing the reliability of theoretical and applied research in high-strain-rate phenomena.

The novelty of our approach lies in its integration of several advanced Bayesian techniques tailored to the challenges of shock loading data. First, the use of Gaussian Process Regression (GPR) to regularize shock wave profiles and estimate strain rates (Sec. IV) addresses the systemic bias inherent in waveform analysis, providing statistically informed estimates of $\dot{\epsilon}$ with quantified uncertainties. This method, applied to expand the fcc Al dataset, has enabled a more comprehensive analysis than was possible with the original sparse data used by Swegle and Grady.² Second, the hierarchical Bayesian model (Sec. VI) explicitly accounts for inter-run variability by allowing source-specific parameters C_j and p_j to vary while sharing common hyperpriors, thus capturing the multi-modal structure of the data (e.g., peaks at $\ln \dot{\epsilon} \sim 10, 15, 20$) that arises from experimental heterogeneity. The adoption of Student's t-likelihood further enhances the model's robustness by accommodating the heavy-tailed nature of the data ($\mu_v = 2.912$), as evidenced by improved Q-Q plots and Pareto k -diagnostics (all $k < 0.7$). This combination of techniques represents a significant departure from traditional least squares fitting, which lacks the tools to assess model adequacy beyond basic error estimates, and offers a more nuanced understanding of the power law's applicability.

The motivation behind this approach stems from the need to move beyond simplistic error minimization techniques that fail to capture the complexity of shock loading data. As highlighted in the introduction, the Swegle–Grady law's empirical foundation is surprisingly sparse, with early analyses relying on limited data points (e.g., three for vanadium³), making them susceptible to fortuitous scaling. Moreover, the presence of inter-run and systemic biases—such as those introduced by VISAR data processing or variations in experimental design—necessitates a statistical framework capable of quantifying these effects. Our Bayesian methodology, underpinned by Markov Chain Monte Carlo (MCMC) sampling, provides a

rigorous means to update beliefs about the power-law parameters in light of the data, offering posterior distributions that reflect both the data's variability and the model's uncertainty. This approach seems to confirm the presence of a power-law relationship, but contrary to prior suggestions, makes the exponent material-dependent, potentially indicating a different universality class or unmodeled physics such as temperature or strain rate dependencies. Future studies focusing on strain rates above 10^9 s^{-1} , where homogeneous defect nucleation dominates, may reveal a more universal scaling relation, as material strengthening effects become less significant under such conditions.

Looking forward, the Bayesian framework developed in this study holds immense potential for future research in shock compression and related fields. First, it can be extended to other materials beyond Al or Fe, such as ceramics, polymers, and amorphous solids, to test the universality of the power law across a broader range of material classes. The hierarchical MCMC approach developed here allows for the inclusion of additional covariates—such as temperature, polycrystallinity, or strain rate history—as demonstrated by prior studies,^{25,31} which could further elucidate the physical mechanisms driving the observed scaling. Second, the methodology can be applied to validate and refine visco-plastic models used in shock loading simulations,^{10,11} ensuring they align with experimental data by satisfying the power-law benchmark. Third, the GPR-based regularization of shock wave profiles can be adapted to other experimental contexts where waveform analysis is critical, such as in seismic studies or ultrasonic testing, providing a robust means to estimate derivatives with quantified uncertainties. Additionally, the Bayesian approach can be used to design future experiments by identifying optimal conditions to minimize inter-run biases, leveraging posterior predictive checks to prioritize data collection strategies that reduce multi-modality in the observed distributions. Finally, this framework can be extended to other universality class problems in physics, such as critical phenomena or fracture mechanics, where experimental variability and sparse data pose similar challenges. By providing a statistically rigorous means to test hypotheses, quantify uncertainties, and account for biases, our Bayesian methodology paves the way for more accurate and informed investigations into the fundamental physics of materials under extreme conditions, ultimately advancing both theoretical understanding and practical applications in material science.

28 June 2025 08:07:12

ACKNOWLEDGMENTS

This work was supported by the Engineering and Physical Sciences Research Council as part of the project *Predictive Multiscale Modelling Protocol of Adiabatic Shear Band Initiation in Manufacturing and Aerospace Materials* (Grant No. EP/W01579X/1). The computations described in this paper were performed using the University of Birmingham's BlueBEAR HPC service.

AUTHOR DECLARATIONS

Conflict of Interest

The authors have no conflicts to disclose.

Author Contributions

Beñat Gurrutxaga-Lerma: Conceptualization (equal); Data curation (equal); Formal analysis (equal); Funding acquisition (equal); Investigation (equal); Methodology (equal); Project administration (equal); Resources (equal); Software (equal); Validation (equal); Visualization (equal); Writing – original draft (equal); Writing – review & editing (equal).

DATA AVAILABILITY

The data that support the findings of this study are available from the corresponding author upon reasonable request.

APPENDIX: HYPERPARAMETER SELECTION FOR COMPOSITE GAUSSIAN PROCESS KERNELS

To accommodate the non-smooth and potentially singular behavior exhibited in the data, particularly near discontinuities, we employed a composite kernel for Gaussian Process Regression (GPR) comprising a convex combination of a Radial Basis Function (RBF) kernel and a Matérn kernel. The resulting covariance function takes the form

$$k(x, x') = C[\alpha k_{\text{RBF}}(x, x'; \ell_{\text{RBF}}) + (1 - \alpha) k_{\text{Matérn}}(x, x'; \ell_{\text{Matérn}}, v)], \quad (\text{A1})$$

where C denotes the signal variance, ℓ denotes the characteristic length scales of the component kernels, $\alpha \in (0, 1)$ is the mixing weight, and v is the smoothness parameter of the Matérn kernel. The RBF component captures highly localized variations, while the Matérn component introduces rougher structure appropriate for modeling non-differentiable transitions.

In standard GPR pipelines, kernel hyperparameters such as length scales and signal variance are estimated by Type-II maximum likelihood, i.e., by maximizing the log marginal likelihood

$$\log p(\mathbf{y} | \mathbf{X}, \theta) = -\frac{1}{2}\mathbf{y}^\top(K_\theta + \sigma_n^2 I)^{-1}\mathbf{y} - \frac{1}{2}\log|K_\theta + \sigma_n^2 I| - \frac{n}{2}\log 2\pi, \quad (\text{A2})$$

where K_θ is the covariance matrix defined by the kernel with hyperparameters θ , and σ_n^2 is the observation noise variance.

However, implementations such as scikit-learn typically treat certain kernel shape parameters—notably v and α —as fixed. These parameters critically influence the model's ability to adapt to discontinuities. To overcome this, we implemented a model selection routine wherein α and v are discretized and explored by grid search, with the remaining hyperparameters optimized via marginal likelihood at each configuration.

The selection procedure proceeds as follows:

1. Define a grid with $\alpha \in \{0.1, 0.3, 0.5, 0.7, 0.9\}$ and $v \in \{0.5, 1.5, 2.5\}$.
2. For each (α, v) pair:
 - (a) Construct the composite kernel as above.

- (b) Fit the GPR model using marginal likelihood optimization of the free hyperparameters (length scales, signal variance).
 - (c) Record the maximized log marginal likelihood.
3. Select the configuration that achieves the highest marginal likelihood.

This hybrid approach maintains automatic hyperparameter learning while enabling empirical selection of structural parameters that critically affect model capacity in non-stationary or low-regularity regimes. The final kernel chosen by this method demonstrated superior predictive stability near discontinuities and avoided the over-smoothing or oscillatory artifacts typically observed with naïve kernel configurations.

REFERENCES

- ¹Y. B. Zel'dovich and Y. P. Raizer, *Physics of Shock Waves and High-Temperature Hydrodynamic Phenomena* (Dover, Mineola, NY, 2002).
- ²J. W. Swegle and D. E. Grady, “Shock viscosity and the prediction of shock wave rise times,” *J. Appl. Phys.* **58**(2), 692–701 (1985).
- ³D. E. Grady, “Structured shock waves and the fourth-power law,” *J. Appl. Phys.* **107**, 013506 (2010).
- ⁴J. W. Swegle and D. E. Grady, “Calculation of thermal trapping in shear bands,” in *Metallurgical Applications of Shock-Wave and High-Strain Rate Phenomena*, edited by K. P. Staudhammer, L. E. Murr, and M. A. Meyers (Taylor & Francis, 1986), Chap. 37, pp. 705–722.
- ⁵F. Reif, *Fundamentals of Statistical and Thermal Physics*, Physics Series (McGraw-Hill, London, 1998).
- ⁶G. B. Rybicki and A. P. Lightman, *Radiative Processes in Astrophysics* (John Wiley & Sons, New York, 1991).
- ⁷J. D. Jackson, *Classical Electrodynamics* (Wiley, New York, 1999).
- ⁸B. Gurrutxaga-Lerma, “The multipolar elastic fields of ellipsoidal and polytopal plastic inclusions,” *Proc. R. Soc. A* **479**(2276), 20230214 (2023).
- ⁹D. E. Grady, “Strain-rate dependence of the effective viscosity under steady-wave shock compression,” *Appl. Phys. Lett.* **38**(10), 825–826 (1981).
- ¹⁰A. Molinari and G. Ravichandran, “Fundamental structure of steady plastic shock waves in metals,” *J. Appl. Phys.* **95**(4), 1718–1732 (2004).
- ¹¹R. A. Austin and D. L. McDowell, “A dislocation-based constitutive model for viscoplastic deformation of fcc metals at very high strain rates,” *Int. J. Plast.* **27**(1), 1–24 (2011).
- ¹²M. A. Shehadeh and H. M. Zbib, “On the homogeneous nucleation and propagation of dislocations under shock compression,” *Philos. Mag.* **96**(26), 2752–2778 (2016).
- ¹³S. Yao, J. Yu, Y. Cui, X. Pei, Y. Yu, and Q. Wu, “Revisiting the power law characteristics of the plastic shock front under shock loading,” *Phys. Rev. Lett.* **126**(8), 085503 (2021).
- ¹⁴Y. Horie, “Observations on the fourth-power scaling of high-pressure shock waves in solids,” *J. Appl. Phys.* **130**(24), 245901 (2021).
- ¹⁵D. E. Grady, “Principles underlying the fourth power nature of structured shock waves,” *AIP Conf. Proc.* **1979**, 070014 (2018).
- ¹⁶L. M. Barker, C. D. Lundergan, and W. Herrmann, “Dynamic response of aluminum,” *J. Appl. Phys.* **35**(4), 1203–1212 (1964).
- ¹⁷G. I. Kanel, S. V. Razorenov, K. Baumung, and J. Singer, “Dynamic yield and tensile strength of aluminum single crystals at temperatures up to the melting point,” *J. Appl. Phys.* **90**(1), 136–143 (2001).
- ¹⁸H. Huang and J. R. Asay, “Compressive strength measurements in aluminum for shock compression over the stress range of 4–22 GPa,” *J. Appl. Phys.* **98**(3), 033524 (2005).
- ¹⁹B. L. Holian and P. S. Lomdahl, “Plasticity induced by shock waves in nonequilibrium molecular-dynamics simulations,” *Science* **280**, 2349–2352 (1998).

- ²⁰S. C. Schmidt, J. W. Shaner, G. A. Samara, and M. Ross, "High-pressure science and technology—1993," Technical Report, New York, NY (AIP Publishing LLC, 1994).
- ²¹L. Davison, Y. Horie, and M. Shahinpoor, *High-Pressure Shock Compression of Solids IV: Response of Highly Porous Solids to Shock Loading* (Springer Science & Business Media, 2012).
- ²²S. Zhuang, G. Ravichandran, and D. E. Grady, "An experimental investigation of shock wave propagation in periodically layered composites," *J. Mech. Phys. Solids* **51**(2), 245–265 (2003).
- ²³T. J. Vogler, J. P. Borg, and D. E. Grady, "On the scaling of steady structured waves in heterogeneous materials," *J. Appl. Phys.* **112**(12), 123507 (2012).
- ²⁴A. Griewank and A. Walther, *Evaluating Derivatives: Principles and Techniques of Algorithmic Differentiation*, 2nd ed. (SIAM, Philadelphia, IL, 2008).
- ²⁵V. H. Whitley, S. D. McGrane, D. E. Eakins, C. A. Bolme, D. S. Moore, and J. F. Bingert, "The elastic-plastic response of aluminum films to ultrafast laser-generated shocks," *J. Appl. Phys.* **109**(1), 013505 (2011).
- ²⁶*LASL Shock Hugoniot Data*, Los Alamos Series on Dynamic Material Properties, edited by S. P. Marsh (University of California Press, LA, 1980), Vol. 5.
- ²⁷M. A. Meyers, *Dynamic Behavior of Materials* (John Wiley, Hoboken, NJ, 1994).
- ²⁸M. A. Meyers, "A model for elastic precursor waves in the shock loading of polycrystalline metals," *Mater. Sci. Eng.* **30**(2), 99–111 (1977).
- ²⁹N. K. Bourne, J. C. F. Millett, and G. T. Gray III, "On the shock compression of polycrystalline metals," *J. Mater. Sci.* **44**, 3319–3343 (2009).
- ³⁰J. T. Lloyd, J. D. Clayton, R. Becker, and D. L. McDowell, "Simulation of shock wave propagation in single crystal and polycrystalline aluminum," *Int. J. Plast.* **60**, 118–144 (2014).
- ³¹E. B. Zaretsky and G. I. Kanel, "Dynamic response of Sn over the temperature range 115–503 K," in *9th DYMAT International Conference* (EDP Sciences, Brussels, 2009), pp. 27–33.
- ³²D. B. Miracle and O. N. Senkov, "A critical review of high entropy alloys and related concepts," *Acta Mater.* **122**, 448–511 (2017).
- ³³B. G. Mullet, J. Korenaga, and S.-I. Karato, "Markov chain Monte Carlo inversion for the rheology of olivine single crystals," *J. Geophys. Res.: Solid Earth* **120**(5), 3142–3172, <https://doi.org/10.1002/2014JB011845> (2015).
- ³⁴Y. Kuhn, H. Wolf, A. Latz, and B. Horstmann, "Bayesian parameterization of continuum battery models from featurized electrochemical measurements considering noise," *Batter. Supercaps* **6**(1), e202200374 (2023).
- ³⁵A. Gelman, J. B. Carlin, H. S. Stern, and D. B. Rubin, *Bayesian Data Analysis* (Chapman and Hall, 1995).
- ³⁶C. P. Robert and G. Casella, *Monte Carlo Statistical Methods*, Springer Texts in Statistics, 2nd ed. (Springer, New York, 2004).
- ³⁷C. E. Rasmussen and C. K. I. Williams, *Gaussian Processes for Machine Learning*, Adaptive Computation and Machine Learning (MIT Press, Cambridge, MA, 2006).
- ³⁸This is not the case any longer in model comparison. Different models will have different marginal likelihoods, and these values are directly compared to assess which model is more supported by the data. In this context, $p(D)$ is no longer a mere normalizing constant but a crucial quantity that influences the comparison of models through the Bayes factor.
- ³⁹D. Frenkel and B. Smit, *Understanding Molecular Simulation: From Algorithms to Applications*, Computational Sciences Series Vol. 1, 2nd ed. (Academic Press, London, 2002).
- ⁴⁰P. Rowe, G. Csányi, D. Alfè, and A. Michaelides, "Development of a machine learning potential for graphene," *Phys. Rev. B* **97**(5), 054303 (2018).
- ⁴¹J. Korenaga and S.-I. Karato, "A new analysis of experimental data on olivine rheology," *J. Geophys. Res.: Solid Earth* **113**(B2), B02403, <https://doi.org/10.1029/2007JB005100> (2008).
- ⁴²C. Jain, J. Korenaga, and S.-I. Karato, "On the yield strength of oceanic lithosphere," *Geophys. Res. Lett.* **44**(19), 9716–9722, <https://doi.org/10.1002/2017GL075043> (2017).
- ⁴³C. Jain, J. Korenaga, and S.-I. Karato, "Global analysis of experimental data on the rheology of olivine aggregates," *J. Geophys. Res.: Solid Earth* **124**(1), 310–334, <https://doi.org/10.1029/2018JB016558> (2019).
- ⁴⁴N. Metropolis, A. W. Rosenbluth, M. N. Rosenbluth, A. H. Teller, and E. Teller, "Equation of state calculations by fast computing machines," *J. Chem. Phys.* **21**(6), 1087–1092 (1953).
- ⁴⁵S. Geman and D. Geman, "Stochastic relaxation, Gibbs distributions, and the Bayesian restoration of images," *IEEE Trans. Pattern Anal. Mach. Intell.* **6**(6), 721–741 (1984).
- ⁴⁶S. Duane, A. D. Kennedy, B. J. Pendleton, and D. Roweth, "Hybrid Monte Carlo," *Phys. Lett. B* **195**(2), 216–222 (1987).
- ⁴⁷R. M. Neal, *Monte Carlo Implementation*, Bayesian Learning for Neural Networks (Springer, 1996), pp. 55–98.
- ⁴⁸S. Brooks, A. Gelman, G. Jones, and X.-L. Meng, *Handbook of Markov Chain Monte Carlo* (CRC Press, Boca Raton, FL, 2011).
- ⁴⁹M. D. Hoffman, A. Gelman *et al.*, "The no-u-turn sampler: Adaptively setting path lengths in Hamiltonian Monte Carlo," *J. Mach. Learn. Res.* **15**(1), 1593–1623 (2014); available at <http://jmlr.org/papers/v15/hoffman14a.html>.
- ⁵⁰For a give strain rate, the difference between the experimentally measured stress and the stress predicted by the fitted model.
- ⁵¹W. T. Eadie, D. Drijard, F. E. James, M. G. W. Roos, and B. Sadoulet, *Statistical Methods in Experimental Physics* (North-Holland, Amsterdam, 1971).
- ⁵²A. Vehtari, A. Gelman, and J. Gabry, "Practical Bayesian model evaluation using leave-one-out cross-validation and WAIC," *Statist. Comput.* **27**, 1413–1432 (2017).
- ⁵³T. Hastie, R. Tibshirani, J. H. Friedman, and J. H. Friedman, *The Elements of Statistical Learning: Data Mining, Inference, and Prediction* (Springer, 2009), Vol. 2.
- ⁵⁴W. A. Fuller, *Measurement Error Models* (John Wiley & Sons, 2009).
- ⁵⁵J. J. Moré and D. C. Sorensen, "Computing a trust region step," *SIAM J. Sci. Stat. Comput.* **4**(3), 553–572 (1983).
- ⁵⁶K. Levenberg, "A method for the solution of certain non-linear problems in least squares," *Q. Appl. Math.* **2**(2), 164–168 (1944).
- ⁵⁷D. W. Marquardt, "An algorithm for least-squares estimation of nonlinear parameters," *J. Soc. Ind. Appl. Math.* **11**(2), 431–441 (1963).
- ⁵⁸J. Nocedal and S. J. Wright, *Numerical Optimization* (Springer, 1999).
- ⁵⁹S. Agarwal, K. Mierle *et al.*, "Ceres solver: Tutorial & reference," Google Inc 2(72), 8 (2012); available at <https://github.com/ceres-solver/ceres-solver>.
- ⁶⁰A. C. Mitchell and W. J. Nellis, "Shock compression of aluminium, copper and tantalum," *J. Appl. Phys.* **52**(5), 3363–3374 (1981).
- ⁶¹J. R. Asay and L. C. Chhabildas, "Paradigms and challenges in shock wave research," in *High-Pressure Shock Compression of Solids VI*, edited by Y. Horie, L. Davison, and N. Thadani (Springer-Verlag, New York, 2003), Chap. 2, pp. 57–119.
- ⁶²J. R. Asay and L. M. Barker, "Interferometric measurement of shock-induced internal particle velocity and spatial variations of particle velocity," *J. Appl. Phys.* **45**(6), 2540–2546 (1974).
- ⁶³J. R. Asay, "Shock loading and unloading in bismuth," *J. Appl. Phys.* **48**(7), 2832–2844 (1977).
- ⁶⁴J. R. Asay, "Shock wave paradigms and new challenges," *AIP Conf. Proc.* **620**, 26–35 (2002).
- ⁶⁵M. B. Boslough and J. R. Assay, "Basic principles of shock compression," in *High Pressure Shock Compression of Solids*, edited by J. R. Asay and M. Shahinpoor (Springer, New York, 1993), Chap. 2, pp. 7–42.
- ⁶⁶H. Huang and J. R. Asay, "Reshock and release response of aluminum single crystal," *J. Appl. Phys.* **101**(6), 063550 (2007).
- ⁶⁷E. B. Zaretsky, G. I. Kanel, S. V. Razorenov, and K. Baumung, "Impact strength properties of nickel-based refractory superalloys at normal and elevated temperatures," *Int. J. Impact Eng.* **31**(1), 41–54 (2005).
- ⁶⁸E. B. Zaretsky, "Impact response of cobalt over the 300–1400 K temperature range," *J. Appl. Phys.* **108**(8), 083525 (2010).
- ⁶⁹E. B. Zaretsky and G. I. Kanel, "Plastic flow in shock-loaded silver at strain rates from 10^4 s^{-1} to 10^7 s^{-1} and temperatures from 296 K to 1233 K," *J. Appl. Phys.* **110**(7), 073502 (2011).

- ⁷⁰E. B. Zaretsky and G. I. Kanel, "Effect of temperature, strain, and strain rate on the flow stress of aluminum under shock-wave compression," *J. Appl. Phys.* **112**(7), 073504 (2012).
- ⁷¹E. B. Zaretsky and G. I. Kanel, "Response of copper to shock-wave loading at temperatures up to the melting point," *J. Appl. Phys.* **114**(8), 083511 (2013).
- ⁷²G. V. Garkushin, G. I. Kanel, and S. V. Razorenov, "Resistance to deformation and fracture of aluminum AD1 under shock-wave loading at temperatures of 20 and 600 °C," *Phys. Solid State* **52**, 2369–2375 (2010).
- ⁷³E. B. Zaretsky and G. I. Kanel, "Tantalum and vanadium response to shock-wave loading at normal and elevated temperatures. Non-monotonic decay of the elastic wave in vanadium," *J. Appl. Phys.* **115**(24), 243502 (2014).
- ⁷⁴E. B. Zaretsky and G. I. Kanel, "Invariance of rate dependences of normalized flow stress in niobium and molybdenum under conditions of shock compression," *J. Appl. Phys.* **120**(10), 105901 (2016).
- ⁷⁵E. B. Zaretsky and G. I. Kanel, "The high temperature impact response of tungsten and chromium," *J. Appl. Phys.* **122**(11), 115901 (2017).
- ⁷⁶E. B. Zaretsky and G. I. Kanel, "Abnormal temperature effects on the dynamic yield stress of alpha-brass," *J. Appl. Phys.* **124**(4), 045902 (2018).
- ⁷⁷E. B. Zaretsky and G. I. Kanel, "Response of poly (methyl methacrylate) to shock-wave loading at elevated temperatures," *J. Appl. Phys.* **126**(8), 085902 (2019).
- ⁷⁸G. I. Kanel, S. V. Razorenov, A. Bogatch, A. V. Utkin, V. E. Fortov, and D. E. Grady, "Spall fracture properties of aluminum and magnesium at high temperatures," *J. Appl. Phys.* **79**(11), 8310–8317 (1996).
- ⁷⁹G. I. Kanel, S. V. Razorenov, E. B. Zaretsky, B. Herrman, and L. Meyer, "Thermal "softening" and "hardening" of titanium and its alloy at high strain rates of shock-wave deforming," *Phys. Solid State* **45**, 656–661 (2003).
- ⁸⁰R. A. Austin, "Elastic precursor wave decay in shock-compressed aluminum over a wide range of temperature," *J. Appl. Phys.* **123**(3), 035103 (2018).
- ⁸¹J. M. Winey, B. M. LaLone, P. B. Trivedi, and Y. M. Gupta, "Elastic wave amplitudes in shock-compressed thin polycrystalline aluminum samples," *J. Appl. Phys.* **106**, 073508 (2009).
- ⁸²J. C. F. Millett, S. J. Fensin, G. D. Owen, B. P. Eftink, C. Lear, G. Whiteman, and G. T. Gray III, "The mechanical and microstructural response of single crystal aluminium to one dimensional shock loading: The effects of orientation," *Acta Mater.* **246**, 118727 (2023).
- ⁸³G. I. Kanel, W. J. Nellis, A. S. Savinykh, S. V. Razorenov, and A. M. Rajendran, "Response of seven crystallographic orientations of sapphire crystals to shock stresses of 16–86 GPa," *J. Appl. Phys.* **106**(4), 043524 (2009).
- ⁸⁴F. Cao, I. J. Beyerlein, F. L. Addessio, B. H. Sencer, C. P. Trujillo, E. K. Cerreta, and G. T. Gray III, "Orientation dependence of shock-induced twinning and substructures in a copper bicrystal," *Acta Mater.* **58**(2), 549–559 (2010).
- ⁸⁵J. P. Escobedo, E. K. Cerreta, D. Dennis-Koller, C. P. Trujillo, and C. A. Bronkhorst, "Influence of boundary structure and near neighbor crystallographic orientation on the dynamic damage evolution during shock loading," *Philos. Mag.* **93**(7), 833–846 (2013).
- ⁸⁶G. I. Kanel, S. V. Razorenov, G. V. Garkushin, S. I. Ashitkov, P. S. Komarov, and M. B. Agranat, "Deformation resistance and fracture of iron over a wide strain rate range," *Phys. Solid State* **56**, 1569–1573 (2014).
- ⁸⁷C. M. Cady, G. T. Gray, S.-R. Chen, R. D. Field, D. R. Korzekwa, R. S. Hixson, and M. F. Lopez, "Influence of temperature, strain rate and thermal aging on the structure/property behavior of uranium 6 wt% Nb," *J. Phys. IV* **134**, 203–208 (2006).
- ⁸⁸O. T. Strand, L. V. Berzins, D. R. Goosman, W. W. Kuhlow, P. D. Sargis, and T. L. Whitworth, "Velocimetry using heterodyne techniques," *SPIE Proc.* **5580**, 593–599 (2005).
- ⁸⁹D. H. Dolan and T. Ao, "SIRHEN: A data reduction program for photonic Doppler velocimetry measurements," Technical Report SAND2010-3628, Sandia National Laboratories, Alburquerque, NM, 2010.
- ⁹⁰F. Reuter, J. Mur, J. Petelin, R. Petkovsek, and C.-D. Ohl, "Shockwave velocimetry using wave-based image processing to measure anisotropic shock emission," *Phys. Fluids* **36**(1), 017127 (2024).
- ⁹¹N. K. Bourne, "Materials' physics in extremes: Akrology," *Metal. Mater. Trans. A* **42**(10), 2975–2984 (2011).
- ⁹²L. Davison, *Fundamentals of Shock Wave Propagation in Solids*, Shock Wave and High Pressure Phenomena (Springer, Berlin, 2008).
- ⁹³C. Williams and C. Rasmussen, "Gaussian processes for regression," in *Advances in Neural Information Processing Systems*, edited by D. Touretzky, M. C. Mozer, and M. Hasselmo (MIT Press, 1995), Vol. 8.
- ⁹⁴D. J. C. MacKay, *Information Theory, Inference and Learning Algorithms* (Cambridge University Press, Cambridge, 2003).
- ⁹⁵D. Duvenaud, "Automatic model construction with Gaussian processes," Ph.D. thesis (University of Cambridge, 2014).
- ⁹⁶M. L. Stein, *Interpolation of Spatial Data: Some Theory for Kriging* (Springer Science & Business Media, 1999).
- ⁹⁷T. de Rességuier and M. Hallouin, "Effects of the α - ϵ phase transition on wave propagation and spallation in laser shock-loaded iron," *Phys. Rev. B* **77**(17), 174107 (2008).
- ⁹⁸M. Betancourt and M. Girolami, "Hamiltonian Monte Carlo for hierarchical models," in *Current Trends in Bayesian Methodology with Applications*, edited by S. K. Upadhyay, U. Singh, D. K. Dey, and A. Loganathan (CRC Press, 2015), Chap. 4.
- ⁹⁹Y. G. Wang, M. L. Qi, H. He, and L. Wang, "Spall failure of aluminum materials with different microstructures," *Mech. Mater.* **69**(1), 270–279 (2014).
- ¹⁰⁰Y. M. Gupta, J. M. Winey, P. B. Trivedi, B. M. LaLone, R. F. Smith, J. H. Eggert, and G. W. Collins, "Large elastic wave amplitude and attenuation in shocked pure aluminum," *J. Appl. Phys.* **105**, 036107 (2009).
- ¹⁰¹B. Glam, D. Moreno, S. Eliezer, and D. Eliezer, "Study of dislocation walls evolution during spall in pure aluminum," *AIP Conf. Proc.* **1426**, 987–990 (2012).
- ¹⁰²J. C. Crowhurst, M. R. Armstrong, K. B. Knight, J. M. Zaug, and E. M. Behymer, "Invariance of the dissipative action at ultrahigh strain rates above the strong shock threshold," *Phys. Rev. Lett.* **107**, 144302 (2011).
- ¹⁰³H. Huang and J. R. Asay, "Reshock response of shock deformed aluminum," *J. Appl. Phys.* **100**(4), 043514 (2006).
- ¹⁰⁴H. Shu, S. Fu, X. Huang, H. Pan, F. Zhang, Z. Xie, J. Ye, and G. Jia, "Plastic behavior of aluminum in high strain rate regime," *J. Appl. Phys.* **116**(3), 033506 (2014).
- ¹⁰⁵S. I. Ashitkov, P. S. Komarov, M. B. Agranat, G. I. Kanel, and V. E. Fortov, "Achievement of ultimate values of the bulk and shear strengths of iron irradiated by femtosecond laser pulses," *JETP Lett.* **98**, 384–388 (2013).
- ¹⁰⁶E. B. Zaretsky and G. I. Kanel, "Yield stress, polymorphic transformation, and spall fracture of shock-loaded iron in various structural states and at various temperatures," *J. Appl. Phys.* **117**(19), 195901 (2015).
- ¹⁰⁷H. Shu, X. Huang, H. Pan, J. Ye, F. Zhang, G. Jia, Z. Fang, Y. Tu, Z. Xie, and S. Fu, "Plastic behavior of steel and iron in high strain rate regime," *Int. J. Fract.* **206**, 81–93 (2017).
- ¹⁰⁸T. De Rességuier, E. Lescoute, and D. Loison, "Influence of elevated temperature on the wave propagation and spallation in laser shock-loaded iron," *Phys. Rev. B* **86**(21), 214102 (2012).
- ¹⁰⁹S. I. Ashitkov, V. V. Zhakhovsky, N. A. Inogamov, P. S. Komarov, M. B. Agranat, and G. I. Kanel, "The behavior of iron under ultrafast shock loading driven by a femtosecond laser," *AIP Conf. Proc.* **1793**, 100035 (2017).
- ¹¹⁰J. Tinka Gammel, D. Swift, and T. Tierney, IV, "Shock response of iron on nanosecond time scales," *AIP Conf. Proc.* **706**, 1385–1388 (2004).
- ¹¹¹G. Righi, C. J. Ruestes, C. V. Stan, S. J. Ali, R. E. Rudd, M. Kawasaki, H.-S. Park, and M. A. Meyers, "Towards the ultimate strength of iron: Spalling through laser shock," *Acta Mater.* **215**, 117072 (2021).

28 June 2025 08:07:12